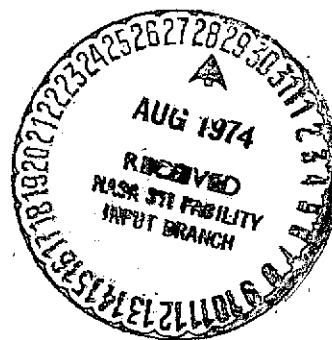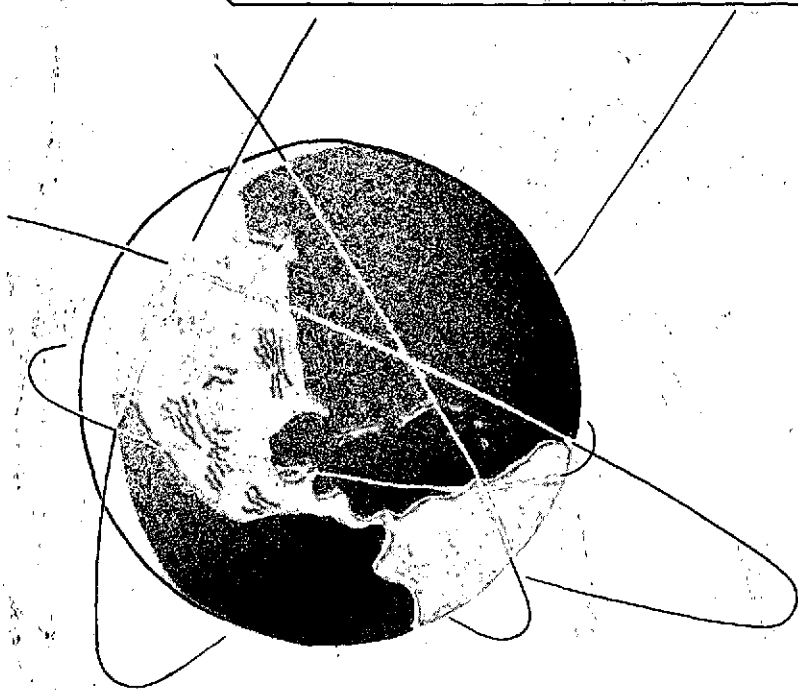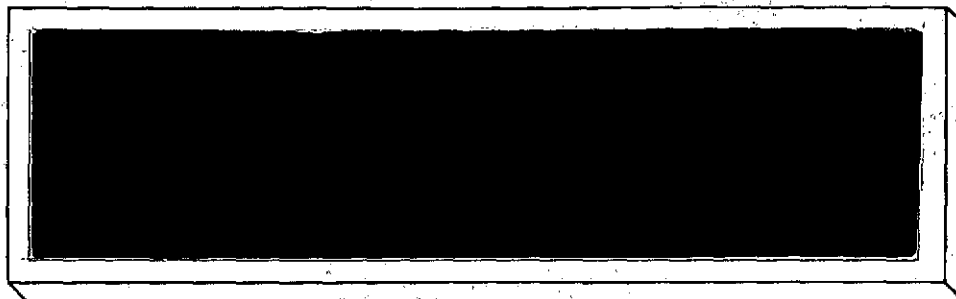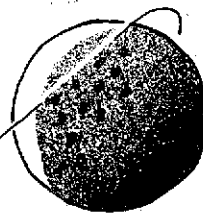NASA CR-134386

(NASA-CR-134386) AN EXPERIMENTAL
INVESTIGATION OF THE FLOW FIELD FOR
DOUBLE-WEDGE CONFIGURATIONS IN A MACH
4.97 STREAM (Texas Univ.) 53 p HC $5.75
CSCL 20D G3/12

N74-30630

Unclas
46378

53

AN EXPERIMENTAL INVESTIGATION OF THE
FLOW-FIELD FOR DOUBLE-WEDGE CONFIGURATIONS
IN A MACH 4.97 STREAM[*]

by John J. Bertin and John C. Hinkle

Aerospace Engineering Report 74003

Department of Aerospace Engineering and
Engineering Mechanics

The University of Texas at Austin
June 1974

i

TABLE OF CONTENTS

INTRODUCTION

To calculate the aerothermodynamic environment for the shuttle entry con-figuration, one must understand and properly model the viscous:inviscid inter-actions for this complex, three-dimensional flow-field. The present investi-gation is concerned with the viscous:inviscid interactions which perturb the flow around the wing leading-edge. The flow-field perturbation results when the fuselage-generated shock wave interacts with the wing-generated shock wave. Based on the flow models of Edney (ref. 1), three types of shock-interference patterns are possible for the wing leading-edge of the orbiter. For small angles of sweep, a Type IV interaction occurs; for intermediate angles of sweep, a Type V interaction occurs; and for a highly swept leading edge, a Type VI interaction occurs. Sketches of these patterns are presented in Fig. 1.

Bertin et al (ref. 2) found that it is possible to generate theoretical solutions both for the Type V and for the Type VI patterns for a given geometry over a wide range of flow conditions. It was not possible to determine from the theoretical solutions which pattern would exist in practice. In addition to questions relating to existence criteria, there are uncertainties regarding the flow model. Graumann (ref. 3) obtained theoretical solutions of the Type V shock-interaction pattern both for perfect-gas properties and for real-gas properties. The calculated pressure rise across the impinging shock wave for the perfect-gas solutions of Graumann differed from the corresponding value reported by Keyes and Hains (ref. 4), even though the shock structure of the flow-field models appeared to be the same.

The experimental program described in the present report was undertaken to determine:

(1)   criteria governing the conditions for which a particular pattern

        exists and

(2) additional information needed to develop flow-field models for

theoretical analysis.

The results of the experimental program conducted in the University of Texas

Supersonic Wind Tunnel are presented in this report. Schlieren photographs,

oil-flow patterns, and surface-pressure measurements were obtained when a

double-wedge configuration was exposed to a supersonic stream. The nominal

flow conditions were a free-stream Mach number of 4.97 with a free-stream

Reynolds number of 0.634×10^6 per cm (19.3×10^6 per foot). The geometric

variables of the program were the deflection angles for the two wedge surfaces.

EXPERIMENTAL PROGRAM

Facility

The tests were conducted in the University of Texas Supersonic Wind Tunnel (UT SWT). The facility is a two-dimensional, blow-down type wind tunnel, using air as the test gas. The nominal dimensions of the test section are width 15.3 cm (6.0 in.) by height 17.8 cm (7.0 in.). The test section diverges slightly along its length to accommodate boundary layer growth.

For the present test program, the free-stream Reynolds number was 0.634×10^6 per cm (19.3×10^6 per foot) at a free-stream Mach number of 4.97. The usable test-time for this Reynolds number is approximately 20 seconds.

Models

A sketch of the double-wedge model used during the test program is shown in Fig. 2. Two different support bases were used so that the effect of the initial wedge angle could be studied. For one model the initial wedge angle (δ) was 5°, for the other it was 15°. The second wedge was intended to represent ("two-dimensionally") the leading-edge of a wing. For each model, the wedge angle varied through a range of sweep angles from 34° to 50°. The dimensions of the model were restricted because of blockage considerations. As shown in Fig. 2, the distance from the leading edge of the first plate to the projected intersection with the second plate was 10.16 cm (4.0 in.). The plate which constituted the (variable-sweep) second wedge was 5.31 cm (2.09 in.) in length. Both plates were 3.18 cm (1.25 in.) in width. During the tests, a constant gap of 0.24 cm (0.092 in.) was maintained between the two wedges to allow for boundary layer bleed off. The gap was used to eliminate the separation bubble which would have formed in the corner (had there been no gap) when the boundary layer on the first wedge encountered the shock-induced adverse pressure gradient.

A total of 37 static pressure orifices were located on the surface of each model: 12 on the first wedge and 25 on the second wedge. The pressure taps were located primarily on the center line of the two surfaces. Because of the restricted model size, three dimensional effects were expected. Therefore, pressure taps were located transversely at two stations on each of the two plates. The specific locations of the pressure taps are illustrated in Fig. 2 and in Table 1. The orifices in the plane of symmetry are first with the other orifices next. The coordinates used are s, the distance from the leading edge (for each plate) and y, the distance from the plane of symmetry.

Two photographs of a typical test setup are presented in Fig. 3. The photographs show the two basic models used in the program, i.e., for one model the initial wedge angle was 5° and for the second model it was 15°. The models were mounted in the test-section using a floor-mounted support system. Leads from the static pressure orifices were taken out of the tunnel aft of the model to a mercury-filled manometer board from which the surface pressure measurements were obtained. Once the mercury levels reached steady state during the run, the pressure leads were sealed (with a knife switch) and the pressures read. The maximum visual error in reading the manometer boards corresponds to a pressure error of $\pm$ 70 N/m^2 ($\pm$ 0.01 psi).

Test Program

The free-stream Mach number for the tests was 4.97 $\pm$ 0.02. The stagnation pressure was 2.16 x 10^6 N/m^2 (309 psia) with a maximum fluctuation during a run of $\pm$ 1.378 x 10^4 N/m^2 ($\pm$ 2 psi). The stagnation temperature range was 294° K (530° R) to 299° K (539° R). As a result, the nominal free-stream Reynolds number was 0.634 x 10^6 per cm (19.3 x 10^6 per foot). Based on the length of the second wedge, this Reynolds number corresponds to a model Reynolds number

$(Re_{\infty,L})$ of 3.37×10^6.

Tests were conducted with initial wedge angles of 5° and 15° and with "leading-edge" sweep angles from 34° to 50°. The data consisted of oil-flow patterns, schlieren photographs, and model surface pressures. The run schedule for those tests in which pressure data were obtained is presented in Table 2. Additional tests were conducted to obtain flow-visualization data only.

DISCUSSION

Theoretical Analysis

The complex flow-field, which is established when a high-speed flow encounters a double-wedge configuration, is dominated by a shock-interaction region which imposes a highly non-uniform flow-field adjacent to the wedge boundary layer. The shock-interference patterns which are of primary interest to the present study are Type V and Type VI. The Type V shock-interaction pattern causes a shock wave to impinge on the wing leading-edge boundary layer, while the Type VI shock-interaction pattern produces an impinging expansion wave.

The flow field model for the Type V interaction (Fig. 4a) includes:

1) the undisturbed free-stream flow,

2) the flow turned through the angle δ by a single shock wave,

3) the flow turned through the angle Λ_s by two shock waves,

4) the flow which has been processed by three shock waves, such that the flow direction and the pressure in region 4 match the corresponding values in region 5,

5) the flow which has been processed by two shock waves, with the second shock wave being a strong shock (with the pressure and flow direction matching those in region 4),

6) the flow which has passed through a curved shock wave, such that the downstream flow is subsonic and parallel to the leading edge of the "simulated wing" (i.e., the second wedge), and

7) the flow turned by a reflected shock wave or by a Mach reflection (i.e., a y-shaped, curved shock wave) depending on the flow condition in region 4 and the shock-wave angle.

The numerical code for the Type V pattern, which is described in ref. 3, is not

6

yet capable of treating the shock:boundary-layer interaction.

The flow-field for the Type VI interaction (Fig. 4b) includes:

1) the undisturbed free-stream flow,

2) the flow turned through the angle δ by a single wave,

3) the flow turned through the angle Λ_s by two shock waves,

4) the flow processed by the right-running waves of the expansion fan which are centered at the intersection of the two shock waves,

5) the flow which passes through the left running waves produced by the reflection of the waves of the expansion fan, and

6) the flow turned through the angle Λ_s by a single shock wave.

The flow in region 3 has passed through two shock waves, while further downstream in region 6 the flow has passed through a single shock wave and is, therefore, at a lower pressure than that in region 3. Thus, although the flow directions are the same, the gas must undergo an expansion from the root region to equalize the pressure. The flow accelerates isentropically through the expansion region so that the pressure and the flow direction in region 5E are identical to the values for region 6. The numerical code for the Type VI interaction is described in ref. 5.

Mechanisms of the Limits of the Shock-Interaction Pattern. Characteristics of the shock-interaction patterns for a double-wedge configuration depend on the deflection angle of the first wedge, the sweep of the second wedge (or simulated "wing") of the model, the free-stream flow condition, and the gas-property model. The minimum leading-edge sweep angle for which a Type V pattern is possible is that for which a linear, oblique shock wave divides region 2 from region 3. The Type VI shock interference characteristics no longer exist when the sweep angle becomes so small that the required outboard flow (i.e., that in region 6) can not be generated by a single, weak shock wave.

Over a range of geometry both the Type V and the Type VI shock-interference patterns can exist numerically for a given geometry subject to a given flow condition. Using the numerical codes developed for the Type V and for the Type VI pattern, either shock-interference pattern could exist over a range of sweep angles. Shapiro (ref. 6) notes that, for a given initial Mach number and for a given turning angle, there may be either a strong shock or a weak shock. The data presented below show that the weaker solution exists experimentally.

Experimental Results

As has been noted, the models were designed such that the initial deflection angle δ could be either $5°$ or $15°$ and the second wedge angle could be set to any desired angle. Obviously the shock wave generated by the $15°$ wedge is stronger than that generated by the $5°$ wedge. Correspondingly, in region 2 (see Fig. 4) the static pressure is higher and the local Mach number is lower for δ of $15°$. The difference in the strength of the impinging shock was sufficient to significantly affect the character of the shock interaction for a given sweep angle of the second wedge. Therefore, the discussion of the experimental results will be divided into two sections: the first reviewing the data for $\delta = 15°$ and the second, the data for $\delta = 5°$.

Initial Deflection Angle of 15°

With the initial deflection angle δ equal to $15°$, all three shock-interaction patterns were obtained over the range of sweep angles tested, i.e., $34°$ to $49.5°$. The schlieren photographs and the static-wall-pressure distributions along the second wedge, i.e., the "simulated" wing leading edge, were used to determine which pattern existed for a given geometry. The minimum sweep angle for which a particular interaction pattern existed experimentally appears in

Table 3.

The experimentally determined ranges are compared with the lower limits as defined in the section "Mechanisms of the Limits of the Shock-Interaction Pattern". The limits represent the values of ref. 7 for a wedge and for a cone. The measured values are in approximate agreement with the values for the two-dimensional wedge flow. Note also that, in the region where either the Type V pattern or the Type VI pattern were theoretically possible, the weaker, Type VI pattern was observed experimentally.

The Type VI results. The schlieren photograph and the static pressure distribution for the second wedge are presented for Run W37 in Fig. 5 and Fig. 6, respectively. Comparing the flow field depicted in the schlieren photograph with the sketch of Fig. 4b, the shock-interaction is a Type VI pattern. Clearly evident in the photograph are: the impinging "bow" shock wave, the linear shock wave dividing region 2 from region 3, the centered expansion fan, the "wing-leading-edge" shock wave, and the shear layer which is approximately parallel to the second wedge and which divides the flow which has passed through two shock waves from the flow which has passed through only one shock wave (i.e., the wing leading-edge shock). Also evident in the schlieren photograph are two weak (Mach) waves which occur when the flow on the second wedge is perturbed by the transverse rows of static orifices. Both perturbations occur in region 3.

Table 3. - The Smallest Sweep Angle for Which a Given Shock-Interaction Pattern Occurs for $\delta = 15°$.

Shock-Interaction Pattern	Measured Λ_{min}	Wedge Theory Λ_{min}	Cone Theory Λ_{min}
Type VI	47°	49.0°	35.5°
Type V	36°	37.7°	24.6°

Thus, the local Mach number in region 3 was calculated using the measured wave angle, i.e., M = 1/sin μ. Experimentally the local Mach number is 1.9 which is equal (to the nearest tenth) to the theoretical value.

The pressure measurements for the second wedge, i.e., the simulated wing leading-edge, are presented in Fig. 6. Also included is the theoretical pressure distribution, as calculated using the numerical code described in ref. 5. The pressure measurements from the plane of symmetry are in good agreement with the theoretical values in region 3. Note that the location where the expansion fan impinges on the surface as determined from the schlieren photograph (which is indicated in Fig. 6 by the upper arrow) is inboard of the theoretical location. The difference between the theoretical and the experimental locations is approximately 0.8 cm. (0.3 in.).

The intersection of the Mach waves emanating from the corner (the lower arrow of Fig. 6) is shown to indicate the limit of the two-dimensional flow in the plane of symmetry. The intersection occurs downstream of the two stations at which orifices were located off the plane of symmetry. At s = 0.24L, the pressure variation in the transverse, or y, direction is 7% of the static pressure measured in the plane of symmetry. At s = 0.48L, the transverse pressure variation is 13%.

Downstream of the interaction perturbed region, i.e., in region 5E, the experimental pressures are somewhat below theory. The difference is attributed to three-dimensional effects.

The Type V results. As noted in the section discussing the limiting mechanisms, when the sweep angle becomes so small that the required outboard flow cannot be generated by a single, weak shock wave, the Type VI pattern is no longer possible. For the present configurations, data first exhibit the characteristics of the Type V shock-interaction pattern when the sweep angle is decreased to 46°. Data

characteristic of the Type V interaction were obtained for sweep angles from just under 47° through 37°.

Schlieren photographs are presented in Fig. 7 for sweep angles of 44° (Run W42), 41° (Run W44), and 37° (Run W61). Although all of these photographs depict the Type V shock-interaction pattern, definite changes in the flow field are evident as the sweep angle is changed. The changes are associated primarily with the shock wave which impinges on the wing leading-edge, dividing region 3 from region 4 in Fig. 4a. Based on the theoretical investigation of ref. 3, it is evident that, as the sweep angle is decreased, the impinging shock wave becomes more normal. The Mach number in region 7 decreases from supersonic values to subsonic values.

At relatively high sweep angles, the flow downstream of the impinging shock is still supersonic and a reflected shock wave is generated. The reflected wave is evident in Fig. 7a, which presents the photograph for Run W42, i.e., $\Lambda = 44°$. The reflected wave is apparently not the simple shock wave which is predicted theoretically when boundary-layer effects are neglected. Instead a complex pattern exists which includes expansion waves and compression waves. This conclusion is based on other data which indicate a "separation bubble" occurs when the impinging shock wave interacts with the boundary layer. Another wave can be seen returning to the surface from the intersection of the reflected wave and the shear layer. This feature is not represented in the current theoretical flow models (refs. 3 and 4). Note also that the physical size of region 5 (refer to Fig. 4a) is very small. For sweep angles nearer the lower limit for which the Type V pattern exists, region 5 was virtually nonexistent. Unfortunately, schlieren photographs for those runs either were not taken or were of poor quality. However, multiple reflections of the impinging wave similar to those appearing in Fig. 7a occurred at the lower sweep angles.

The schlieren photograph for an intermediate Type-V sweep-angle is presented

in Fig. 7b. Theoretically (ref. 3), the impinging shock wave has become so strong that the downstream flow is subsonic. Thus, the pattern corresponds to the Type V flow model with a Mach-wave reflection. However, the experimentally observed pattern is much more complex than the current theoretical flow model. Multiple waves impinge on the surface. Furthermore, although the theoretical Mach number for the downstream flow is subsonic, reflected waves are evident. The waves cross into region 5, which grows in size as the sweep angle decreases.

The schlieren photograph of the flow pattern just prior to transition from the Type V pattern is presented in Fig. 7c. The photograph is for $\Lambda = 37°$, i.e., Run W61. The shock wave which divides region 2 from region 3 has begun to bow. As noted in the section on limiting mechanisms, this indicates the onset of the Type IV pattern. Region 5 has become more extensive. Furthermore, multiple waves originating in this region can be seen impinging on the surface.

The effect of sweep angle on the shock-interaction structure for the Type V pattern has been discussed using the schlieren photographs of Fig. 7. The experimentally observed shock structure for Run 44, i.e., $M_{\infty} = 4.97$, $\delta = 15°$, and $\Lambda = 41°$, is compared in Fig. 8 with the theoretical solution. For a given test condition, the shock-wave angles are uniquely determined by the numerical code described in ref. 3. The computed angle of the wing-root shock wave, i.e., the shock wave dividing region 2 from region 3, is 55°.(with respect to the surface of the initial wedge) while the experimental value is 52°. The difference between the experimental and the theoretical values is attributed to the fact that the actual Mach number in region 2 just upstream of the "wing-root" shock is greater than the theoretical value. This conclusion is based on the static pressure measurements for the first wedge. These pressure data indicate that the flow accelerates along the length of the plate. The pressure near the leading edge is slightly above the theoretical value for a 15° deflection

of the free-stream flow, while the pressure measured near the intersection with the second wedge is slightly below the theoretical value. The difference between the theoretical and the measured values for the wing-root shock-wave angle affects the correlation of the remainder of the shock structure (refer to Fig. 8).

Because the flow field contains both subsonic and supersonic regions, the lengths of the shock-wave elements are not determined by the current numerical code. To compute the geometry of the shock structure, the numerical code requires that one specifies either the length of the shock wave which divides region 2 from region 5 or the surface length of region 3. For the computed geometry presented in Fig. 8, the length of the shock wave dividing region 2 from region 5 was assumed to be equal to the experimentally observed value.

The theoretical values for the angles for the various shock-wave elements correlate well with the experimentally determined values. There is also good agreement between the theoretical and the experimental values for the flow direction in region 4 and in region 5. The correlation can be seen by noting the similarity between the calculated and the observed shear layer dividing region 4 from region 5. Thus, the difference between the calculated and the measured values for the wing-root shock wave contributes significantly to the differences between the flow field computed by the theoretical code and that portrayed in the schlieren photograph. The correlation, however, is considered good.

The theoretical Mach number of 0.42 which is tabulated in Fig. 8 for region 6 applies only to the flow just downstream of the normal portion of the shock wave. Proceding outboard, the wing-leading-edge shock wave weakens rapidly, so that the flow downstream of the shock is again supersonic. The supersonic flow which exists downstream of the wing-leading-edge shock outboard of the interaction region has a significant influence on the flow field, as will be discussed subsequently. The current theoretical flow model assumes the local

Mach number and, therefore, the static pressure are constant in region 7, i.e., the region adjacent to the wall and downstream of the Mach reflection. However, the varying strength of the wing-leading-edge shock noted above affects the flow in region 7.

Photographs of oil flow patterns on the second wedge were obtained over a range of sweep angles. At the relatively high sweep angles (specifically those for which a Type VI pattern exists), no significant information about the shock-interaction structure was obtained from the oil-flow patterns. For those sweep angles for which a Type V pattern exists, oil accumulated in the region where the impinging shock strikes the surface. Photographs of the surface oil-flow patterns are presented in Fig. 9 for sweep angles of 46° and of 41°. Because the trace of the oil-flow accumulation is relatively faint, an arrow is included to help identify the location of the trace in the reproductions. The accumulation of oil becomes more pronounced as the sweep angle decreases. These patterns suggest that the interaction between the impinging shock and the boundary layer produces a separation bubble. The separation bubble grows as the impinging shock wave becomes more normal, i.e., as the sweep angle decreases.

The static-pressure measurements from the second wedge are presented in Fig. 10 over a range of Type V sweep angles. The intersection of the Mach waves emanating from the corners (the arrow of Fig. 10) is shown to indicate the limit of the two-dimensional flow in the plane of symmetry. When the shock impinges in the vicinity of the transverse row of orifices, there is considerable pressure variation in the transverse, or y, direction. Away from the interaction the transverse variation is typically 15% of the static pressure measured in the plane of symmetry. Based on the transverse pressure gradient and on the oil-flow patterns, it is concluded that the three-dimensional effects do not affect the character of the data.

The experimental pressure distribution along the plane of symmetry is compared with the theoretical values computed using the code of ref. 3. As noted previously, the numerical code does not calculate the shock-interaction location without some empirical information. For the calculations presented in Fig. 10, the impingement point for the theoretical pressure distribution was determined from the schlieren photographs. Therefore, the location of the measured shock-induced pressure rise should be the same as the location of the "theoretical" interface between region 3 and region 7. The shock-induced pressure rise does not approach the theoretically predicted jump. Furthermore, the increase is measured at only a few orifices. Since the experimental pressure distribution represents measurements from a finite number of orifices, it is possible to miss the maximum value. It is also possible that the experimentally determined peak pressure is less than it should be, if the orifice size is relatively large compared to the peak pressure region. Thus, the measurement may reflect an averaging of the pressure perturbation. Nevertheless, the pressure data are believed reflect the true character of the shock-interaction structure. The pressure decreases significantly downstream of the impingement, asymptotically approaching a constant value.

The pressure rise produced by the impinging shock wave is less than the theoretical rise and affects only a small region of the wing leading-edge. To gain insight into the causes of these differences, consider the pressure immediately downstream of the wing shock. Referring to Fig. 4a and to Fig. 8, the wing shock is composed of three segments: (1) that which divides region 2 from region 3 (or the "wing-root" shock), (2) that which divides region 2 from region 5, and (3) that which divides region 1 from region 6 (or the "wing-leading-edge" shock). The pressure immediately downstream of the shock was calculated using the shock wave angle measured in Fig. 8 and the theoretical Mach number just upstream of the shock wave. The pressure distribution, thus calculated, is

compared with the data from the plane of symmetry in Fig. 11. In region 3, the pressure calculated using the numerical code of ref. 3 is higher than the data; whereas the calculated pressure behind the shock wave is essentially equal to them. The differences between theory and data have been discussed previously. A sharp increase is evident in the pressure just downstream of the shock which divides region 2 from region 5. Recall that the pressure in region 4 (just downstream of the impinging shock) is equal to the pressure in region 5. Thus, one would expect the pressure in region 7 (just downstream of the reflection) to be even higher. However, the pressure perturbation indicated by the schlieren photograph was not measured, perhaps because of the limited number of orifices of finite size, as noted previously. Outboard of the interaction region, (i.e., for s > 0.5L) the pressure just downstream of the wing-leading-edge shock wave correlates closely with the data. The agreement should be expected since the pressure gradient across the shear layer would be small in the absence of significant curvature of the streamlines. Thus, to properly model the Type V shock-interaction structure one should modify the flow model shown in Fig. 4a.

The Type IV results. As noted in the section "Mechanism of the Limits of the Shock-Interaction Pattern", the breakdown of the Type V pattern occurs when the shock dividing region 2 from region 3 (i.e., the wing-root shock wave) is no longer linear. When the sweep angle was decreased below 36°, the wing-root shock wave becomes significantly curved and the shock-interaction pattern changes markedly (refer to Fig. 1). A schlieren photograph of the Type IV pattern is presented in Fig. 12. The shock wave is curved along the entire length of the second wedge. A shear layer which is essentially parallel to the wing leading-edge and a jet which impinges on the surface can be seen originating in the interaction region.

The pressure measurements for the second wedge are presented in Fig. 13 for Run W46, for which δ = 15° and Λ = 34°. The static wall-pressure is rela-

tively constant near the wing root and outboard of the interaction region. Using the average wave angle from the schlieren photographs, the pressure downstream of the wing-root shock wave is calculated to be 57 times the free-stream value, as shown in Fig. 13. The calculated pressure downstream of the outboard-most trace of the wing-leading-edge shock is approximately 20 times the free-stream value. These "calculated" values provide a reasonable approximation of the measured pressures. The pressure distribution presented in Fig. 13 is similar to those reported by Keyes and Hains (ref. 4). The pressure distribution does not exhibit any local pressure peaks which could be used to compute locally high heat-transfer rates using the relations of Markarian (ref. 8). The locally high heating rates are associated with the impingement of the jet.

The location of the interaction-perturbed region. For a Type VI shock-interaction pattern, the location of the interaction-perturbed region is uniquely defined by the computer code described in ref. 5. However, for a Type V shock-interaction pattern, the numerical code of ref. 3 does not uniquely define the interaction-perturbed region. As noted previously, one must input certain characteristic lengths so that the interaction geometry for the Type V interaction can be computed by the program.

Schlieren photographs, surface-pressure distributions, and oil-flow patterns have been used to determine that region of the second wedge, i.e., the simulated wing leading-edge, which is affected by the shock-interaction. The experimentally determined locations of the interaction perturbed region, which are presented in Fig. 14, represent the upstream end of the perturbed region. The location of the interaction is independent of the technique used. The largest "discrepancies" appear in the locations determined using the pressure data. This is understandable since the pressures were measured at a finite number of specific locations. The test program was conducted in two phases. Run number W59 through W68 represent tests which were intended to supplement the original program.

Over the range of sweep angles tested, the location of the perturbed region moves inboard as the sweep angle decreases. It is interesting to note that the curve is continuous even as the interaction pattern changes character, e.g., from Type VI to Type V. Thus, as the wing-leading-edge shock increases in strength (with a corresponding increase in the downstream pressure) so that the impinging wave goes from an expansion wave (Type VI) to a compression wave (Type V), the impingement location does not change suddenly. The fact that the experimentally-determined interaction location is a "well-behaved" function of sweep will be useful to a numerical solution which requires empirical inputs.

Initial Deflection Angle of 5°

As can be seen in Table 2, pressure data were obtained for fewer sweep angles when $\delta = 5°$ then when $\delta = 15°$. In addition, there were no tests for which only flow-visualization data were obtained. Several factors led to the decision to limit the scope of the test program for model configurations with $\delta = 5°$. The factors included: (1) the flow-visualization photographs were not as graphic and (2) the relatively weak "bow" shock wave muted the shock interaction pattern.

Schlieren photographs are presented in Fig. 15 for sweep angles of 50° (Run W47), of 46° (Run W49), of 43° (Run W53), of 41.5° (Run W54), and of 40° (Run W55). Pressure measurements for these same configurations are presented in Fig. 16. Based on the "Mechanisms of the Limits of the Shock-Interaction Pattern", the minimum sweep angle for which a given shock interaction exists is summarized in Table 4 for $\delta = 5°$. For the sweep angles tested, data characteristic of the

Table 4. - The Smallest Sweep Angle for Which a Given
Shock-Interaction Pattern Occurs for $\delta = 5°$.

Shock-Interaction Pattern	Measured Λ_{min}	Wedge Theory Λ_{min}	Cone Theory Λ_{min}
Type VI	48°	49.0°	35.5°
Type V	47° (approx)	45.0°	31.2°

Type V pattern were not obtained. Thus, the lower limit of the Type V pattern is less than 48° (the smallest sweep angle for which a Type VI pattern was obtained) but greater than 46° (the greatest sweep angle for which a Type IV pattern was obtained). That the Type V pattern should exist only over a brief range of sweep angles when δ = 5° is not surprising. Because the "bow" shock wave is weak, the flow in region 2 is only slightly different from that in region 1. Thus, the minimum deflection angle for which it is possible to have a weak shock wave divide region 1 from region 6 is not much different than the minimum deflection angle for which a weak shock wave dividing region 2 from region 3 is possible.

Schlieren photographs. Schlieren photographs of the flow fields generated for δ = 5° are presented in Fig. 15. As has been noted, the shock wave in the wing-root region is curved for sweep angles of 46°, or less. Thus, for all but the highest sweep angle of Fig. 15 (i.e., for all but Λ = 50°), the shock-interaction pattern is a Type IV pattern.

The Type VI pattern for Λ = 50° (Run W47), which appears in Fig. 15a, is similar to that presented for an initial deflection angle of 15° (in Fig. 5). Evident are: the "bow" shock wave, the "wing-root" shock wave, the centered expansion fan which impinges on the wing leading-edge, the "wing leading-edge" shock wave, and the shear layer which is essentially parallel to the wing leading-edge. Mach waves originating from the transverse rows of pressure taps are visible. The measured wave angle was used to determine the experimental value of the Mach number in region 3. The experimentally determined Mach number is 1.52, which compares favorably with the theoretical value of 1.60 computed using the numerical code described in ref. 5. In addition, the wing-root shock wave, i.e., that dividing region 2 from region 3, is measured to be 50° with respect to the first wedge, whereas the theoretical value is 51.4°.

Because the wing-root shock wave is curved (Figs. 15b through 15e), the shock-interaction pattern is categorized as a Type IV pattern. Otherwise, the photographic trace of the Type IV shock-interaction pattern in Fig. 15b is not very different than the trace of the Type VI pattern in Fig. 15a. Note also that the inflection in the shock wave inboard of the intersection of bow shock wave, which is evident in Fig. 12 (δ = 15°), does not appear in the schlieren photographs for the configurations with δ = 5°. As the sweep angle is decreased, the trace of the jet which impinges on the surface becomes stronger.

Surface-pressure measurements on the second wedge. The surface-pressure measurements for the wing leading-edge are presented in Fig. 16. For Λ = 50° (Fig. 16a), the experimental pressure distribution correlates closely with the theoretical distribution for the Type VI pattern. For region 3, the pressure measurements from the plane of symmetry are in very good agreement with the theoretical value up to the intersection of the Mach waves which emanate from the corners. Thus, the differences between experiment and theory downstream of this point are attributed primarily to three-dimensional effects. The location of the intersection of the expansion fan with the wing leading-edge which was determined using the schlieren photograph (Fig. 15a) is within 0.25 cm. (0.1 in.) of the theoretical location. The static pressure data from region 5E are approximately 15% to 20% below the theoretical level. The data are believed to reflect the fact that the plate is of finite span and that the flow is not actually two dimensional.

For a double-wedge configuration where δ = 5° and Λ = 46°, a Type V shock-interaction pattern is theoretically possible using the numerical code described in ref. 3. However, comparing the experimental pressure distribution with the theoretical solution for a Type V shock-interaction pattern, it is clear that a

Type V shock-interaction pattern did not exist. As was done for Fig. 10, the schlieren photograph was used to locate the interaction-perturbed region on the surface of the wing leading-edge. Instead of the pressure rise associated with a Type V interaction, the pressure decreases continuously. In addition, as noted previously, the fact that the wing-root shock wave is curved supports this conclusion. Note that this is the lone instance during the present program for which the experimentally determined minimum sweep angle for a given pattern was greater than the theoretical minimum calculated using wedge theory (ref. 7).

Thus, it is concluded that for sweep angles from 40° to 46°, the shock-interaction pattern is a Type IV pattern. However, because of the relatively weak bow shock-wave, there is not much difference between the surface pressure inboard of the interaction and that outboard of the interaction. As a result, the pressure variation along the wing leading-edge is gradual, but continuous. The pressure distribution, therefore, differs significantly from that observed for δ = 15° where, as noted previously, the static wall pressure is relatively constant near the wing root and outboard of the interaction.

The location of the interaction-perturbed region. Schlieren photographs have been used to determine that region of the second wedge which is affected by the shock interaction. The experimentally determined locations of the interaction perturbed region, which are presented in Fig. 17, represent the upstream end of the perturbed region. Over the range of sweep angles tested, the location of the perturbed region moves inboard as the sweep decreases. Again, the curve is continuous even as the interaction changes character.

CONCLUDING REMARKS

Over the range of geometries tested in the present program, the following conclusions are made.

1. Whereas theoretical solutions both for a Type V pattern and for a Type VI pattern can be generated for a particular test condition (as defined by the geometry and the free-stream conditions), the weaker shock pattern was observed experimentally.

2. There is satisfactory agreement between the experimentally observed Type VI shock-interaction pattern and the theoretical solution.

3. The correlation between the measured Type V shock-interaction pattern and the theoretical solution is satisfactory up to the region where the interaction intersects the surface. The Type V pattern varied with sweep angle as was predicted by the theoretical model. However, the data indicated deficiencies in the theoretical flow model. The pressure distribution along the simulated wing leading-edge differed significantly from the calculated distribution. The weakening of the leading-edge shock wave outboard of the interaction has a marked effect on the surface pressure.

4. The surface-pressure distribution for the Type IV shock-interaction pattern did not exhibit local pressure increases which would indicate locally severe heat-transfer rates. Thus, to predict the heat-transfer distribution along the wing leading-edge it is necessary to explore the governing flow mechanisms.

5. That portion of the simulated wing leading-edge which is affected by the shock-interaction moves inboard as the sweep angle decreases. The interaction location is a continuous function of sweep angle even as the interaction changes character, i.e., from Type VI to Type V and then to Type IV.

22

REFERENCES

1. Edney, B.: "Anomalous Heat Transfer and Pressure Distributions on Blunt
    Bodies at Hypersonic Speeds in the Presence of an Impinging Shock",
    Report 115, 1968, Flygtechniska Försöksanstalten (The Aeronautical Re-
    search Institute of Sweden).

2. Bertin, J. J., Graumann, B. W., and Goodrich, W. D.: "Analsyis of High-
    Velocity and Real-Gas Effects on the Shock-Interference Pattern for Delta-
    Wing Orbiters", AIAA Paper 74-522, June 1974, AIAA 7th Fluid and Plasma
    Dynamics Conference, Palo Alto, Calif.

3. Graumann, B. W.: "Theoretical Analysis of Shock:Shock Interaction Patterns
    for Two-Dimensional Flow", Master of Science Thesis, January 1974, The
    University of Texas at Austin.

4. Keyes, J. W., and Hains, F. D.: "Analytical and Experimental Studies of
    Shock Interference Heating in Hypersonic Flows", TN D-7139, May 1973, NASA.

5. Bertin, J. J., and Graumann, B. W: "Analysis of a Two-Dimensional Type VI
    Shock-Interference Pattern Using a Perfect-Gas Code and a Real-Gas Code",
    Aerospace Engineering Report ⁷³003, August, 1973, The University of Texas
    at Austin.

6. Shapiro, A. H.: The Dynamics and Thermodynamics of Compressible Fluid Flow,
    Vol. I, The Ronald Press Company, New York, 1954.

7. Ames Research Staff: Equations, Tables, and Charts for Compressible Flow",
    Report 1135, 1953, NACA.

8. Markarian, C. F.: "Heat Transfer in Shock Wave-Boundary Layer Interaction
    Regions", NWC TP 4485, November 1968, Naval Weapons Center.

Table 1. - Location of the static-pressure orifices

Orifice No.	First Wedge s cm(in)	First Wedge y cm(in)	Second Wedge s cm(in)	Second Wedge y cm(in)
1	0.635(0.25)	0.0(0.0)		
2	1.270(0.50)	0.0(0.0)		
3	2.540(1.00)	0.0(0.0)		
4	5.080(2.00)	0.0(0.0)		
5	7.620(3.00)	0.0(0.0)		
6	10.160(4.00)	0.0(0.0)		
7			0.254(0.10)	0.0(0.0)
8			0.508(0.20)	0.0(0.0)
9			0.762(0.30)	0.0(0.0)
10			1.016(0.40)	0.0(0.0)
11			1.270(0.50)	0.0(0.0)
12			1.524(0.60)	0.0(0.0)
13			1.778(0.70)	0.0(0.0)
14			2.032(0.80)	0.0(0.0)
15			2.286(0.90)	0.0(0.0)
16			2.540(1.00)	0.0(0.0)
17			2.794(1.10)	0.0(0.0)
18			3.048(1.20)	0.0(0.0)
19			3.302(1.30)	0.0(0.0)
20			3.556(1.40)	0.0(0.0)
21			3.810(1.50)	0.0(0.0)
22			4.318(1.70)	0.0(0.0)
23			4.826(1.90)	0.0(0.0)
24	1.270(0.50)	0.635(0.25)		
25	1.270(0.50)	1.270(0.50)		
26	10.160(4.00)	0.318(0.125)		
27	10.160(4.00)	0.635(0.25)		
28	10.160(4.00)	0.953(0.375)		
29	10.160(4.00)	1.270(0.50)		
30			1.270(0.50)	0.318(0.125)
31			1.270(0.50)	0.635(0.25)
32			1.270(0.50)	0.953(0.375)
33			1.270(0.50)	1.270(0.50)
34			2.540(1.00)	0.318(0.125)
35			2.540(1.00)	0.635(0.25)
36			2.540(1.00)	0.953(0.375)
37			2.540(1.00)	1.270(0.50)

Table 2. - Schedule for those runs
in which static pressures were measured.

$M_\infty = 4.97$ $Re_{\infty,L} = 3.37 \times 10^6$

$\delta = 5°$	$\delta = 15°$
$\Lambda = 50°$, W47	$\Lambda = 49.5°$, W37
$\Lambda = 48°$, W48	$\Lambda = 47.5°$, W38
$\Lambda = 46°$, W49	$\Lambda = 47°$, W39
$\Lambda = 45.5°$, W50	$\Lambda = 46°$, W40
$\Lambda = 45°$, W51	$\Lambda = 45.5°$, W57
$\Lambda = 44°$, W52	$\Lambda = 45°$, W41
$\Lambda = 43°$, W53	W58
$\Lambda = 41.5°$, W54	$\Lambda = 44°$, W42
$\Lambda = 40°$, W55	$\Lambda = 42.5°$, W43
	$\Lambda = 41°$, W44
	$\Lambda = 39.5°$, W45
	$\Lambda = 34°$, W46

Body

M < 1

"Wing leading-edge" shock

M < 1

M_∞

"Bow" shock

M < 1

"Wing-root" shock

TYPE IV

Jet

Shear layer

"Wing leading-edge" shock

M < 1

M_∞

"Bow" shock

"Wing-root" shock

TYPE V

"Wing leading-edge" shock

Shear layer

Expansion

M_∞

"Bow" shock

TYPE VI

"Wing root" shock
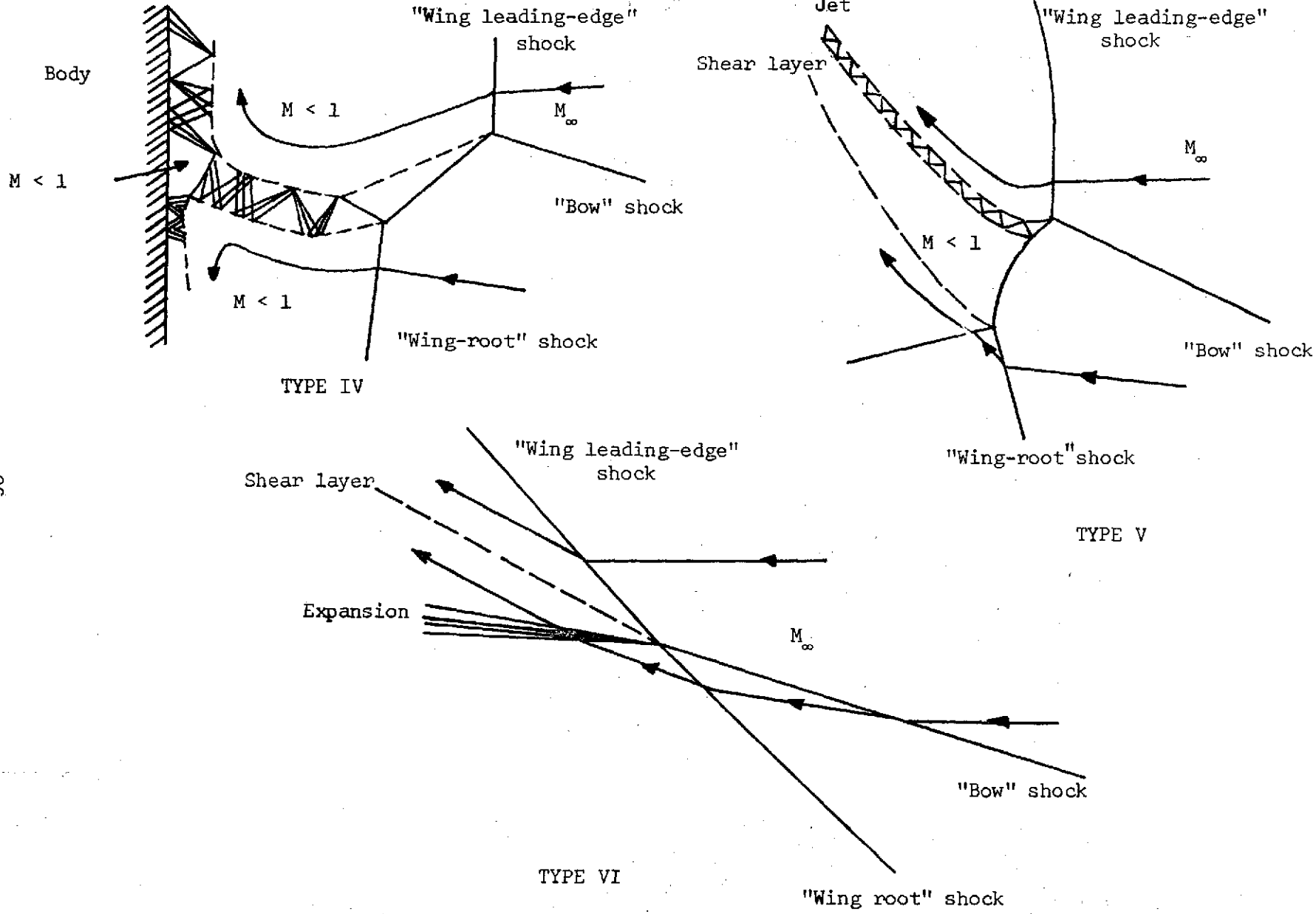
Figure 1. - Sketch of shock-interference patterns as given by Edney (ref. 1).

Note: All dimensions in inches

1.25

2.09

Λ

4.00

δ
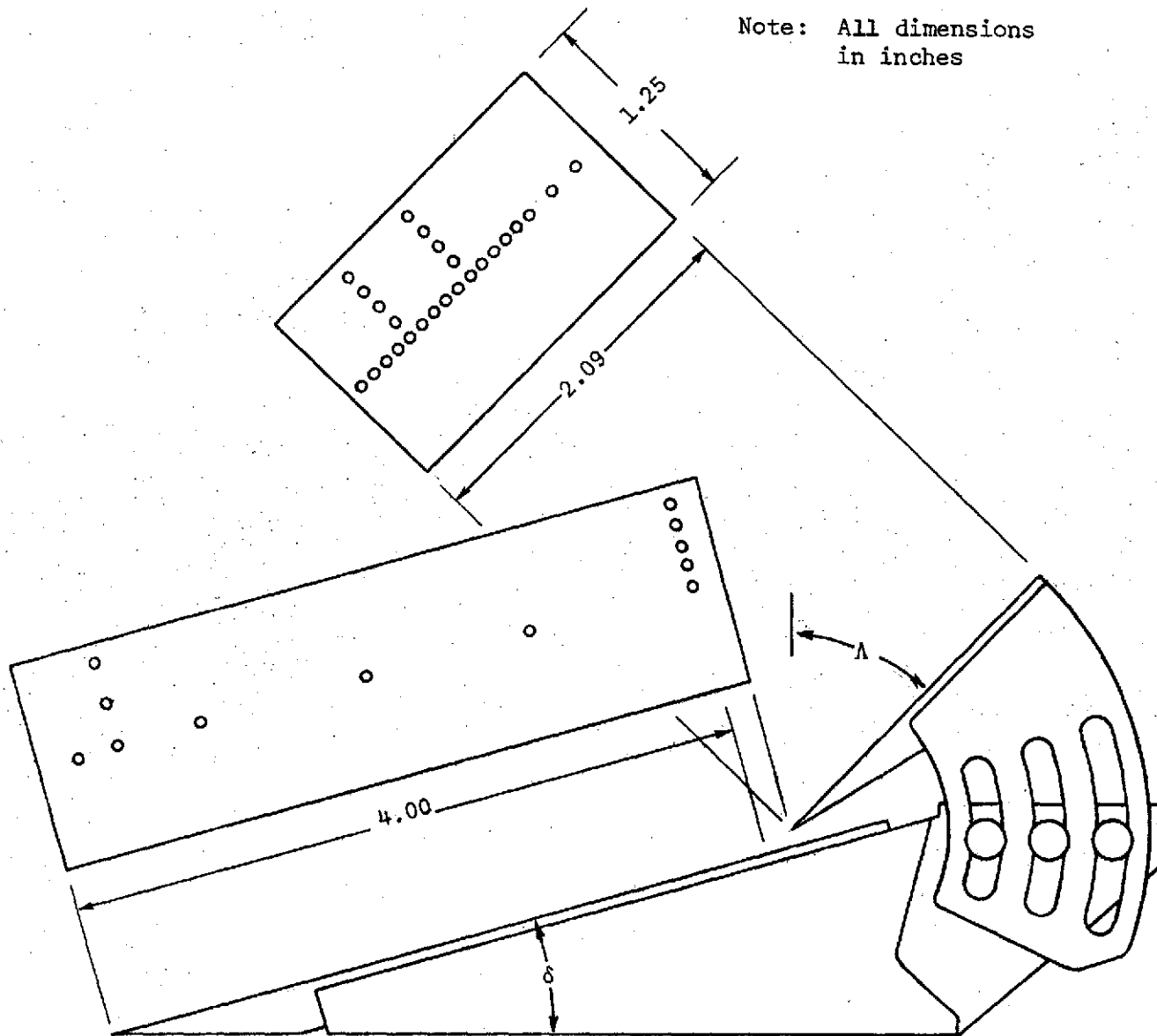
Figure 2. - Sketch of the double-wedge model used in the University's Supersonic Wind Tunnel.

27
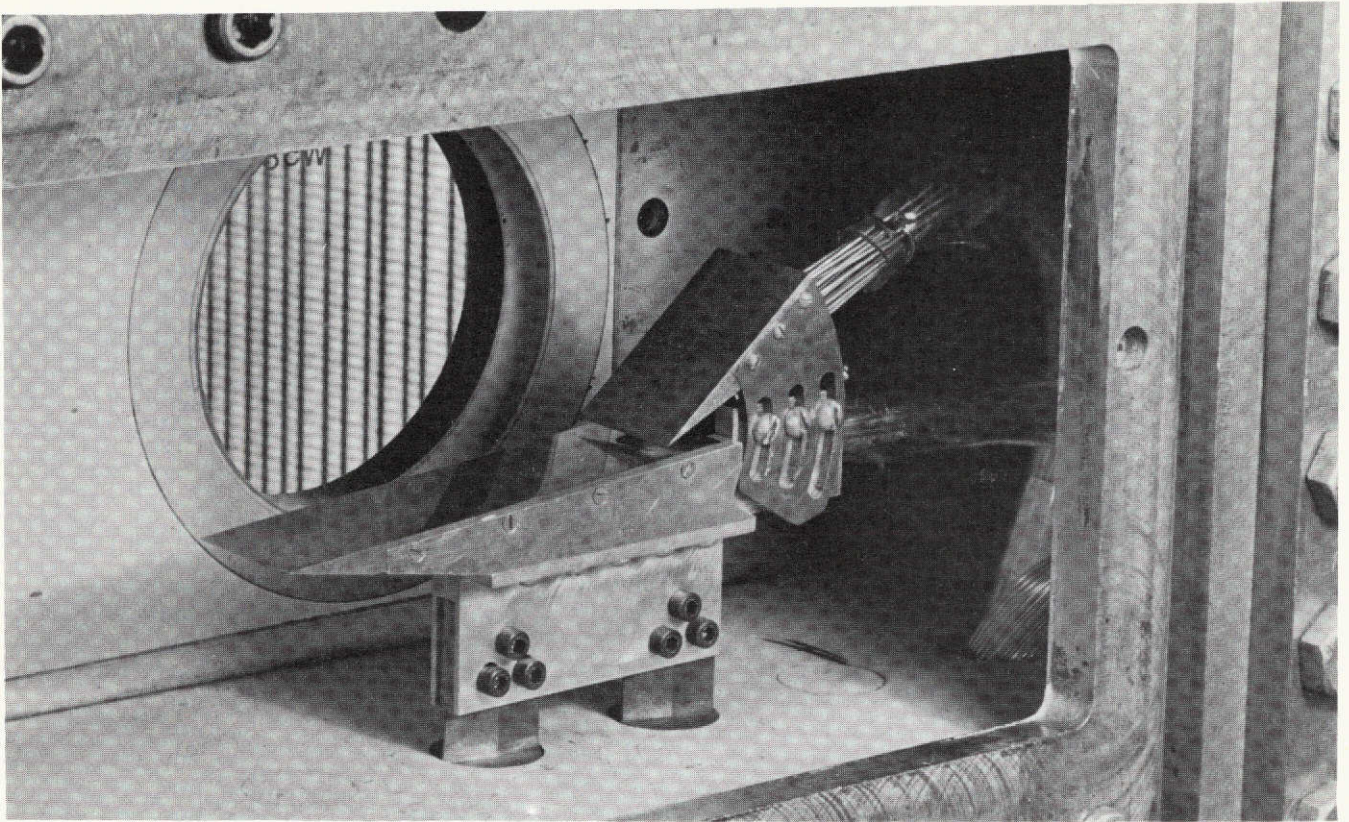
(a) $\delta = 5°$
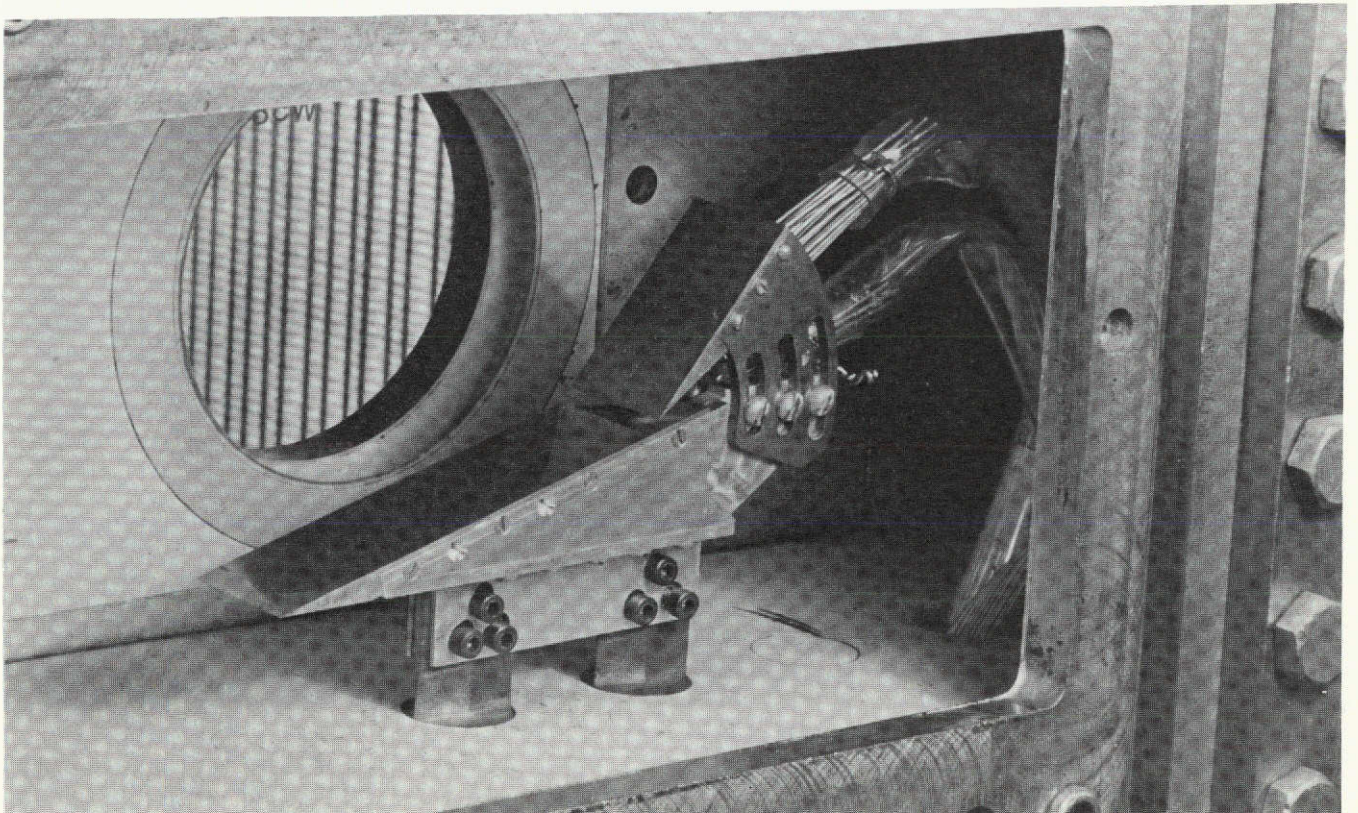
(b) $\delta = 15°$

Figure 3. - Photographs of the two basic models in the UT SWT.

WING LEADING-EDGE SHOCK

FREE-STREAM ①

JET

⑥ ⑦

WING-ROOT SHOCK

⑤ ④

SHEAR LAYER

REFLECTED SHOCK

SHOCK

③

BOW SHOCK

② $\Lambda_s(=90°-\Lambda)$

δ
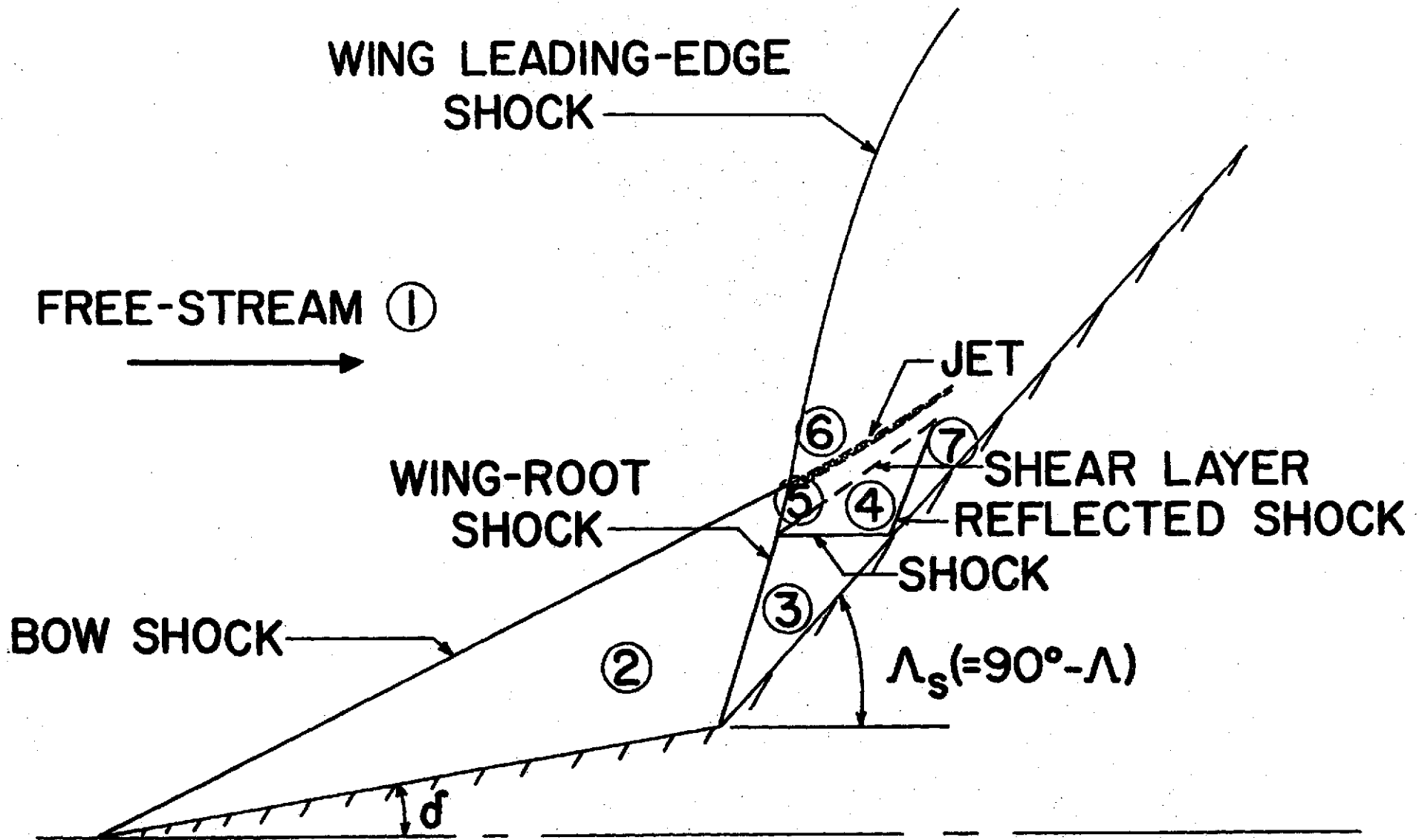
(a) TYPE V

Figure 4. - Flow models of the shock-interaction pattern for a double wedge.

WING LEADING-EDGE SHOCK

SHEAR LAYER

FREE-STREAM ①

CENTERED EXPANSION FAN ④

REFLECTED EXPANSION WAVES ⑤

BOW SHOCK

$\Lambda_s(=90°-\Lambda)$
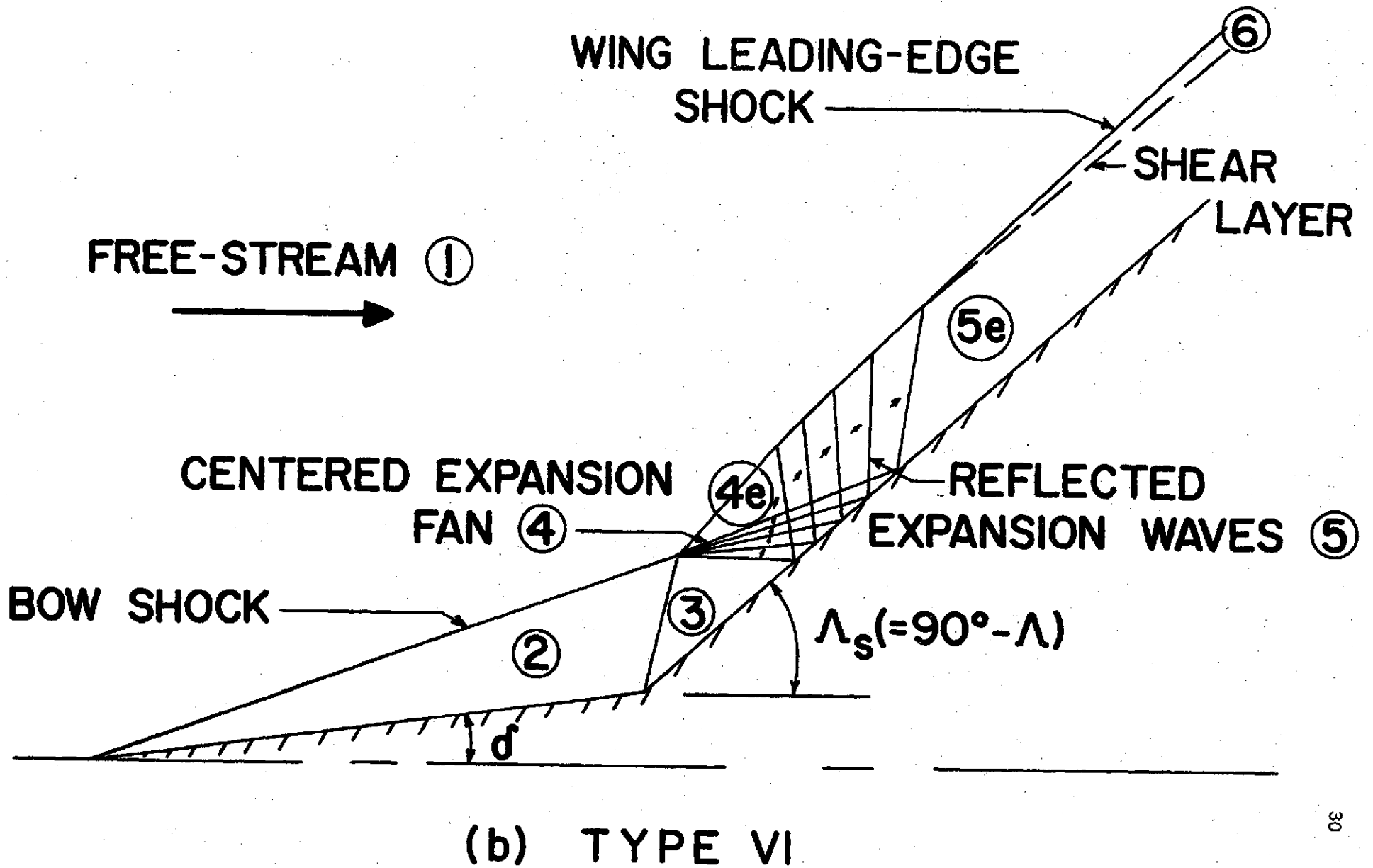
(b) TYPE VI

Figure 4. - Concluded.
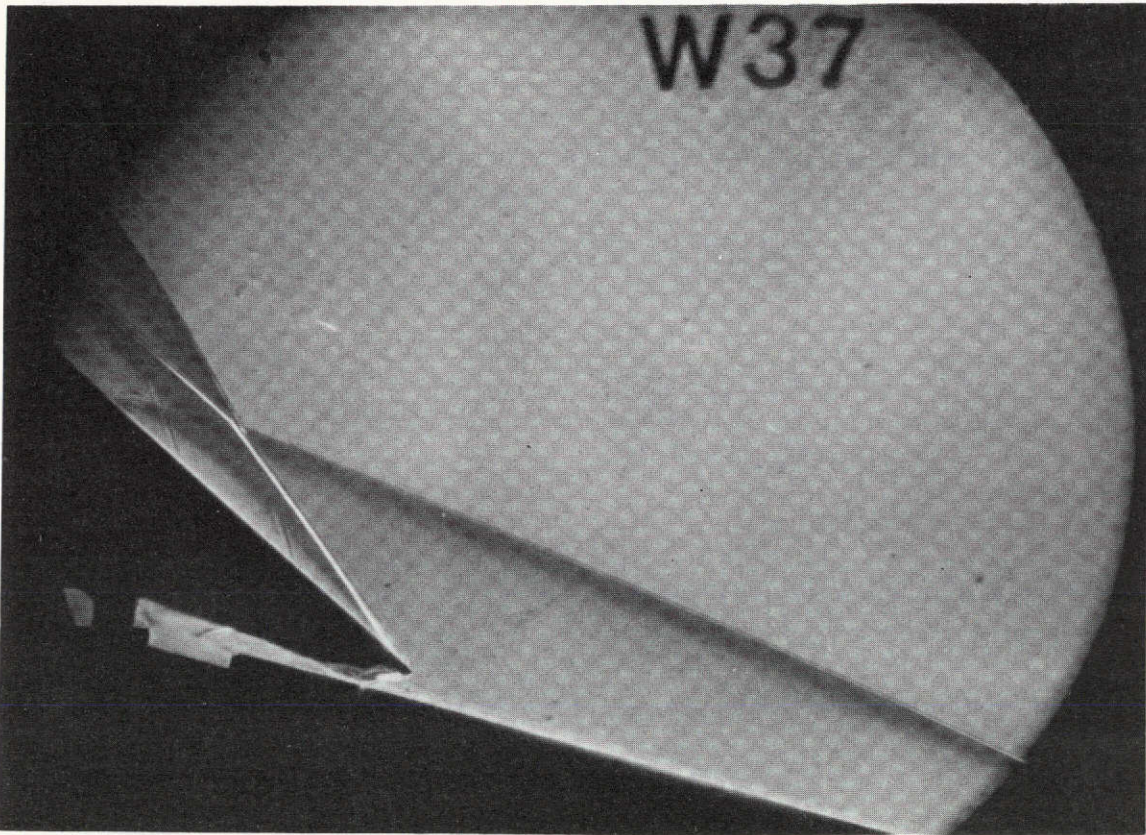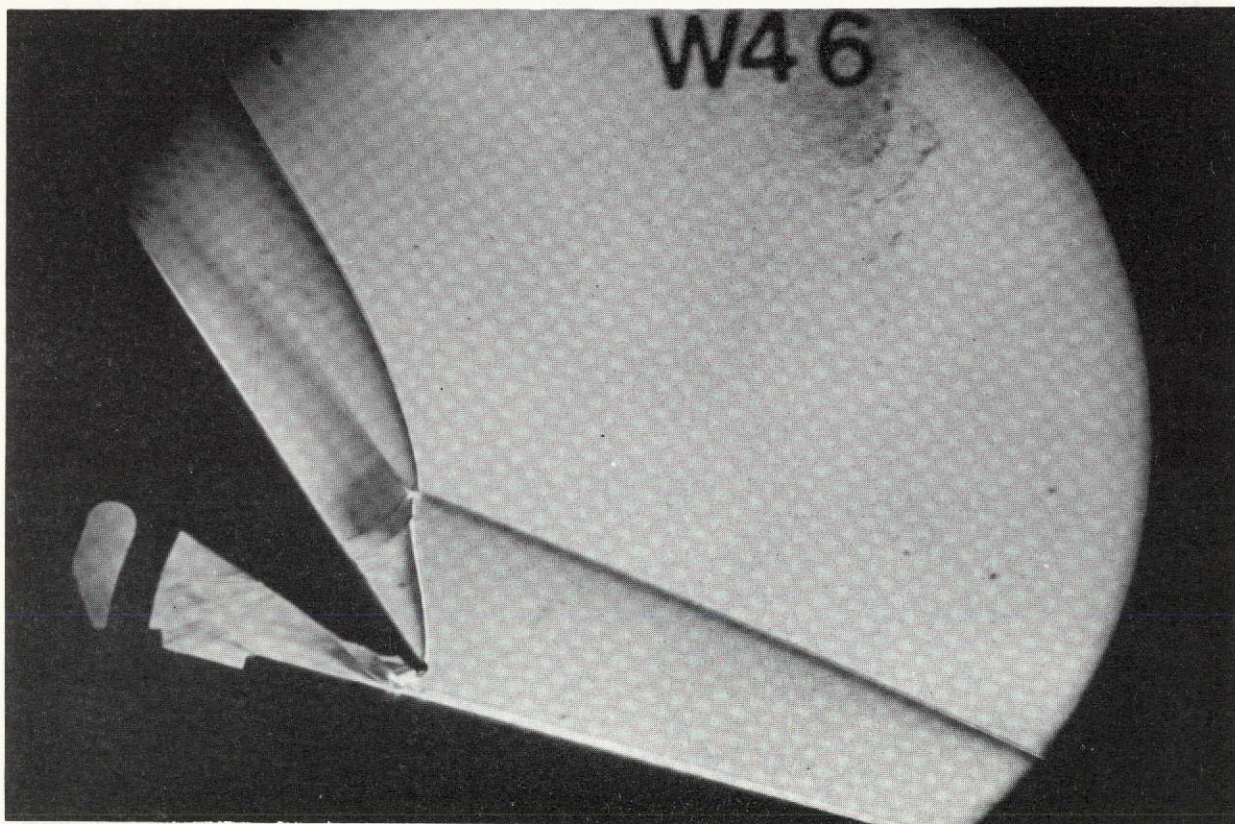
Figure 5. - Schlieren photograph of shock interaction pattern (Type VI) for Run W37, $\delta = 15°$, $\Lambda = 49.5°$.

Figure 6. - Comparison of the experimental and the theoretical pressure distribution along the simulated wing leading edge for a Type VI shock-interaction pattern, Run W37°,$\delta = 15°$, $\Lambda = 49.5°$
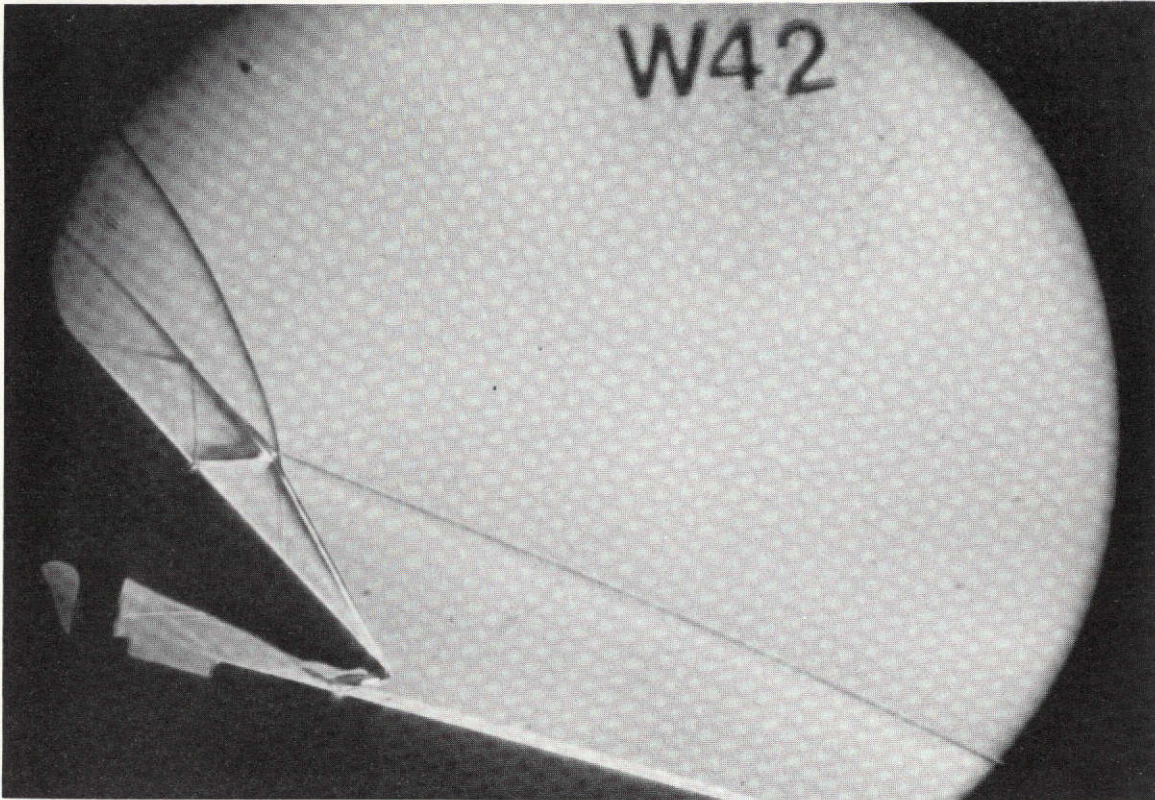
(a) Run W42, $\delta = 15°$, $\Lambda = 44°$
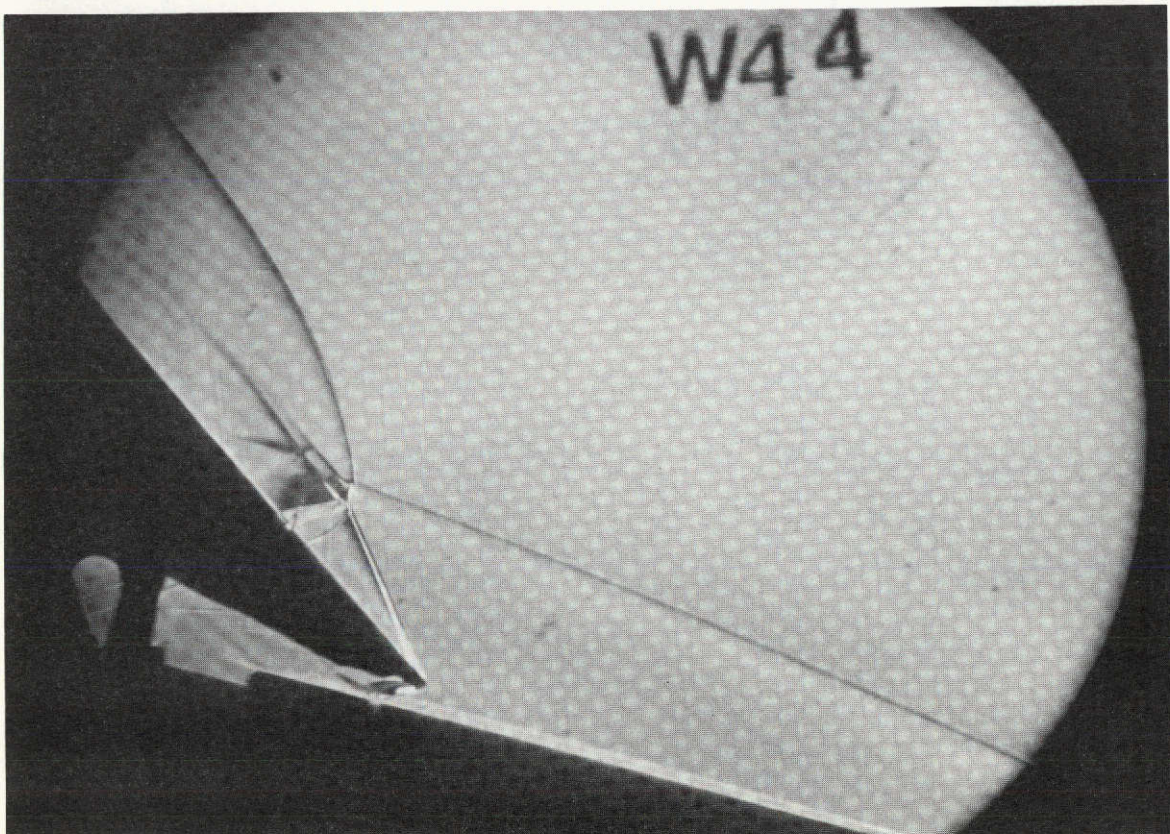
(b) Run W44, $\delta = 15°$, $\Lambda = 41°$

Figure 7. - Schlieren photographs of the Type V shock-interaction pattern for different sweep angles.
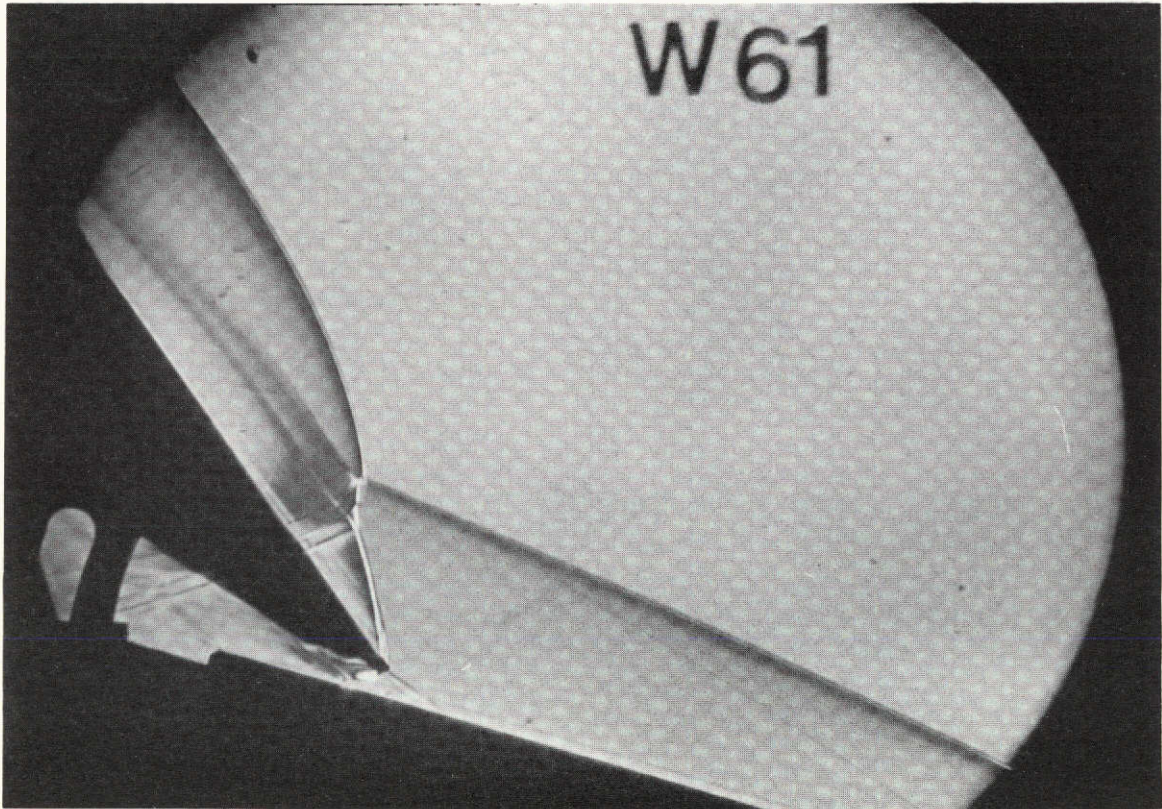
(c) Run W61, $\delta = 15°$, $\Lambda = 37°$

Figure 7. - Concluded.
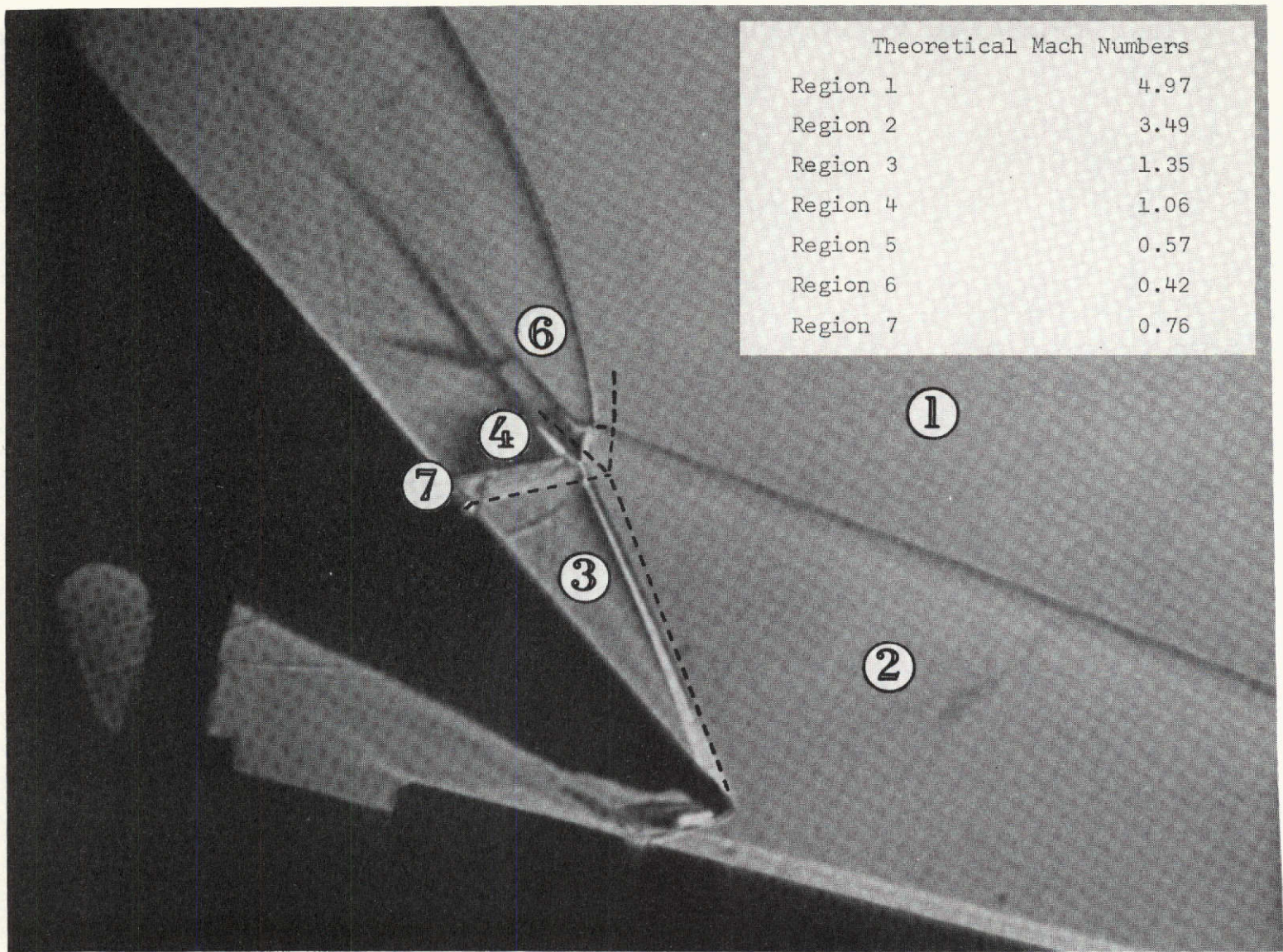
Figure 8. - Comparison of computed flow-field using code of ref. 3 with the schlieren photograph. Run W44, δ = 15°, Λ = 41°.

(a) W67, δ = 15°, Λ = 46°
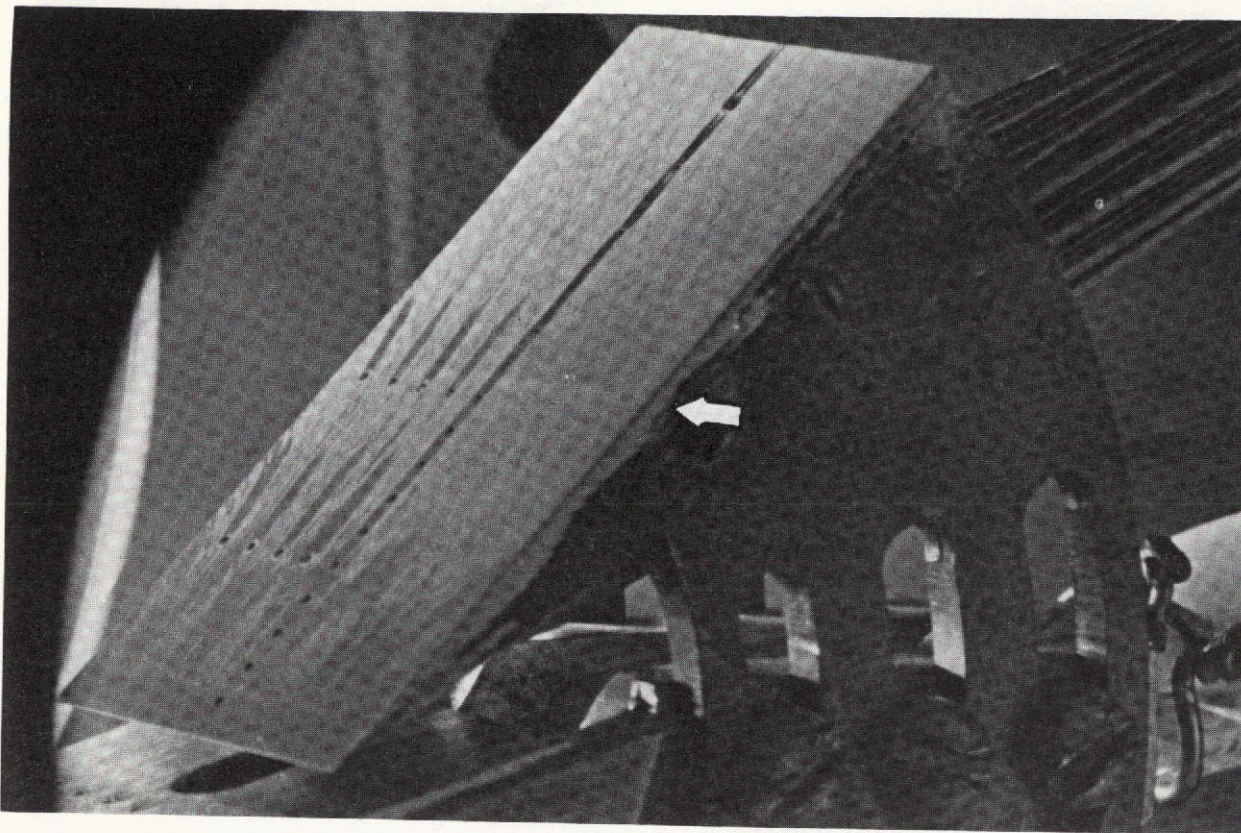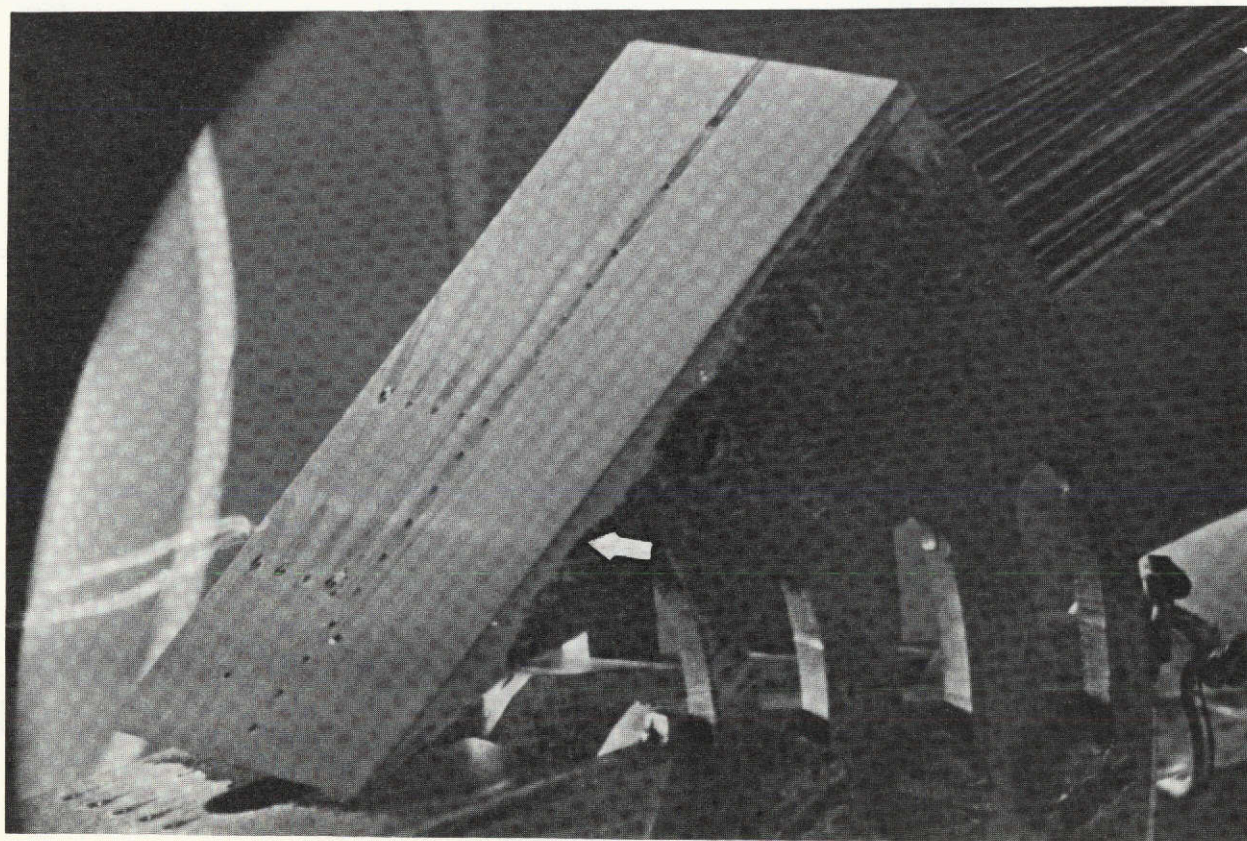
(b) W68, δ = 15°, Λ = 41°

Figure 9. - Oil-flow patterns on the second wedge for the Type V shock interactions.

Figure 10. - Comparison of the experimental and the theoretical pressure distribution along the simulated wing leading edge for a Type V shock-interaction pattern.

(a) Run 40, $\delta = 15°$, $\Lambda = 46°$

(b) Run 57, δ = 15°, Λ = 45.5°

Figure 10. - Continued.

(c) Run W44, δ = 15°, Λ = 41°

Figure 10. – Concluded.

△ Pressure immediately behind the shock determined using the shock wave angle distribution in the schlieren photograph (Fig. 8)

○ Static pressure measured on surface of second wedge
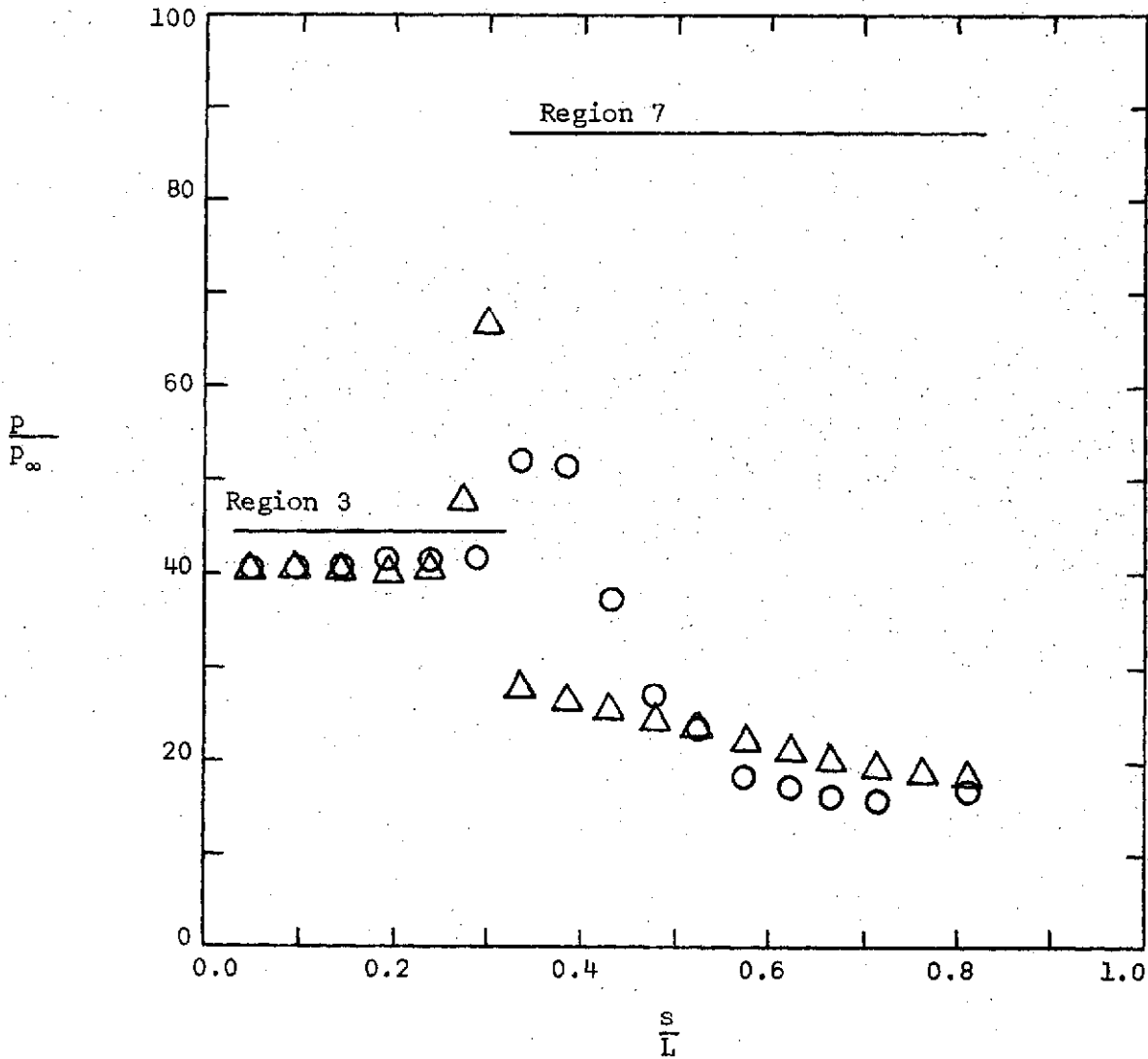
Figure 11. - Comparison of the static pressure distribution along the second wedge with the values immediately downstream of the shock and with the theoretical values. Run W44, $\delta = 15°$, $\Lambda = 41°$.

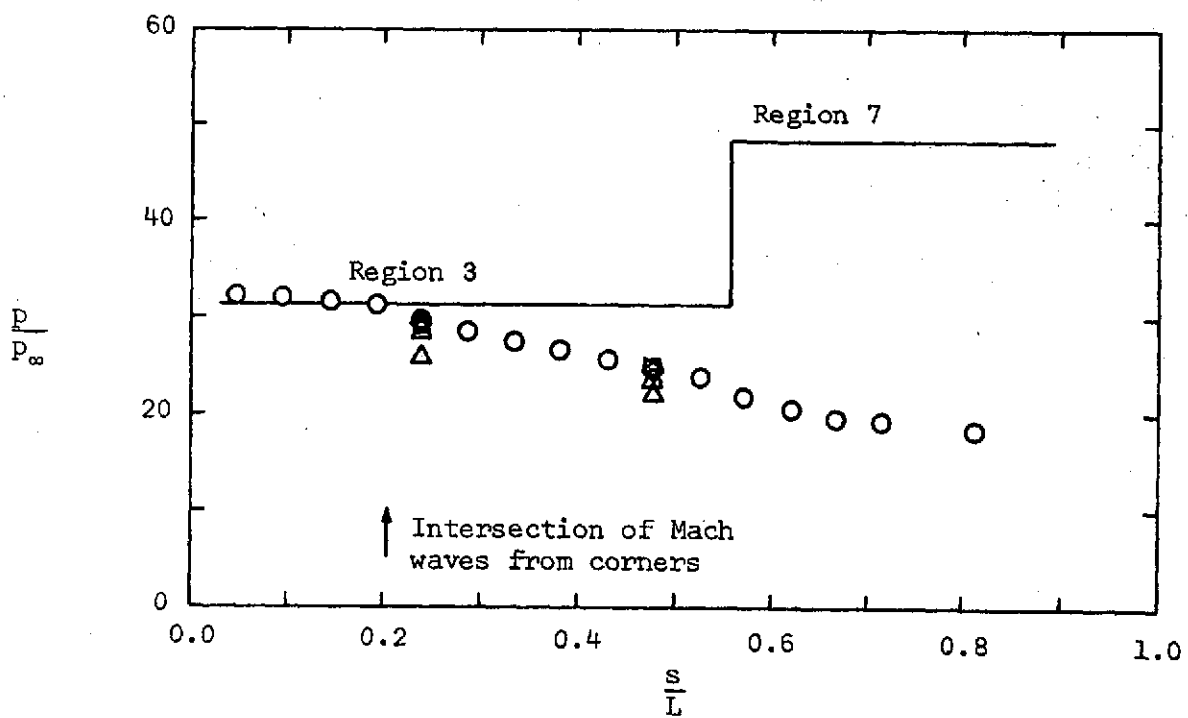Figure 12. - Schlieren photograph of shock interaction pattern (Type IV) for Run W46, $\delta = 15°$, $\Lambda = 34°$.
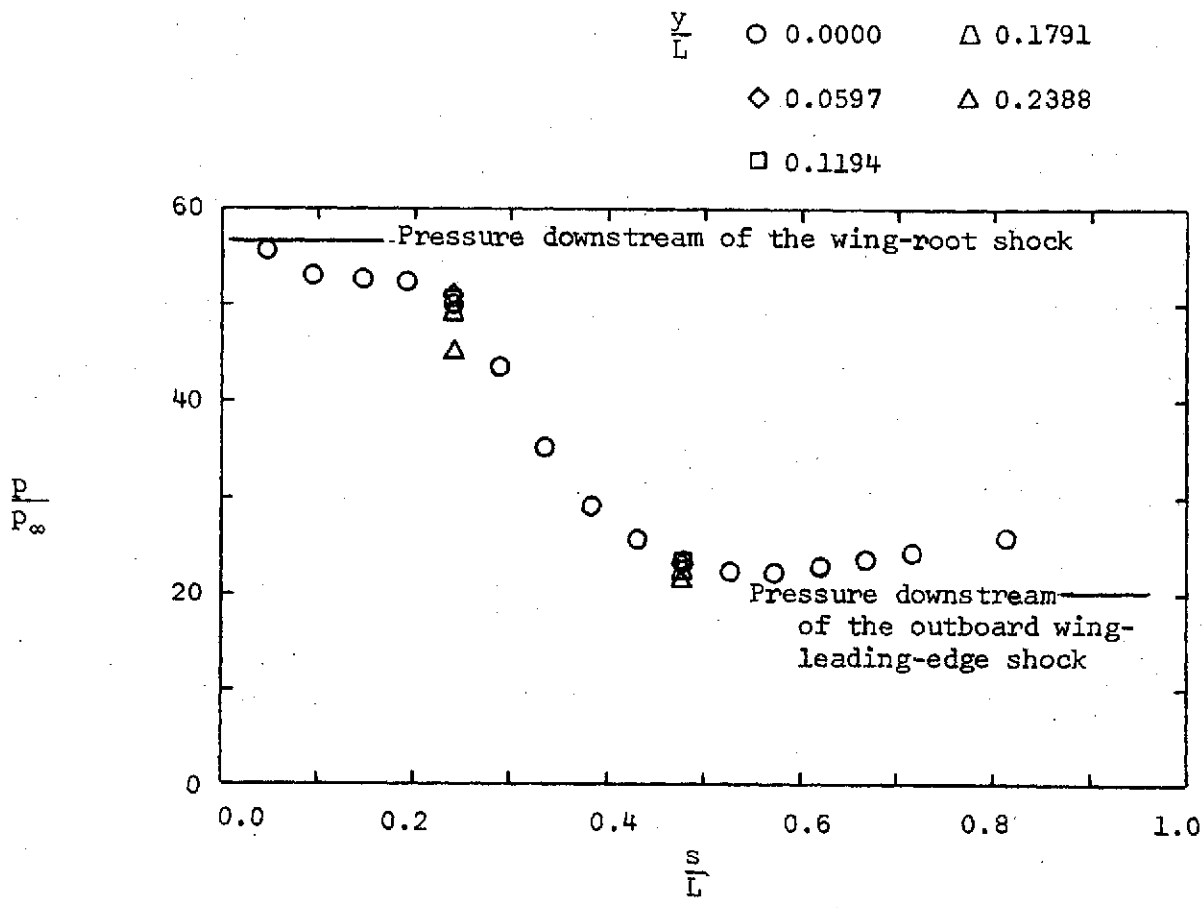
Figure 13. - The pressure distribution along the simulated leading edge for a Type IV shock-interaction patter. Run W46, $\delta = 15°$, $\Lambda = 34°$.
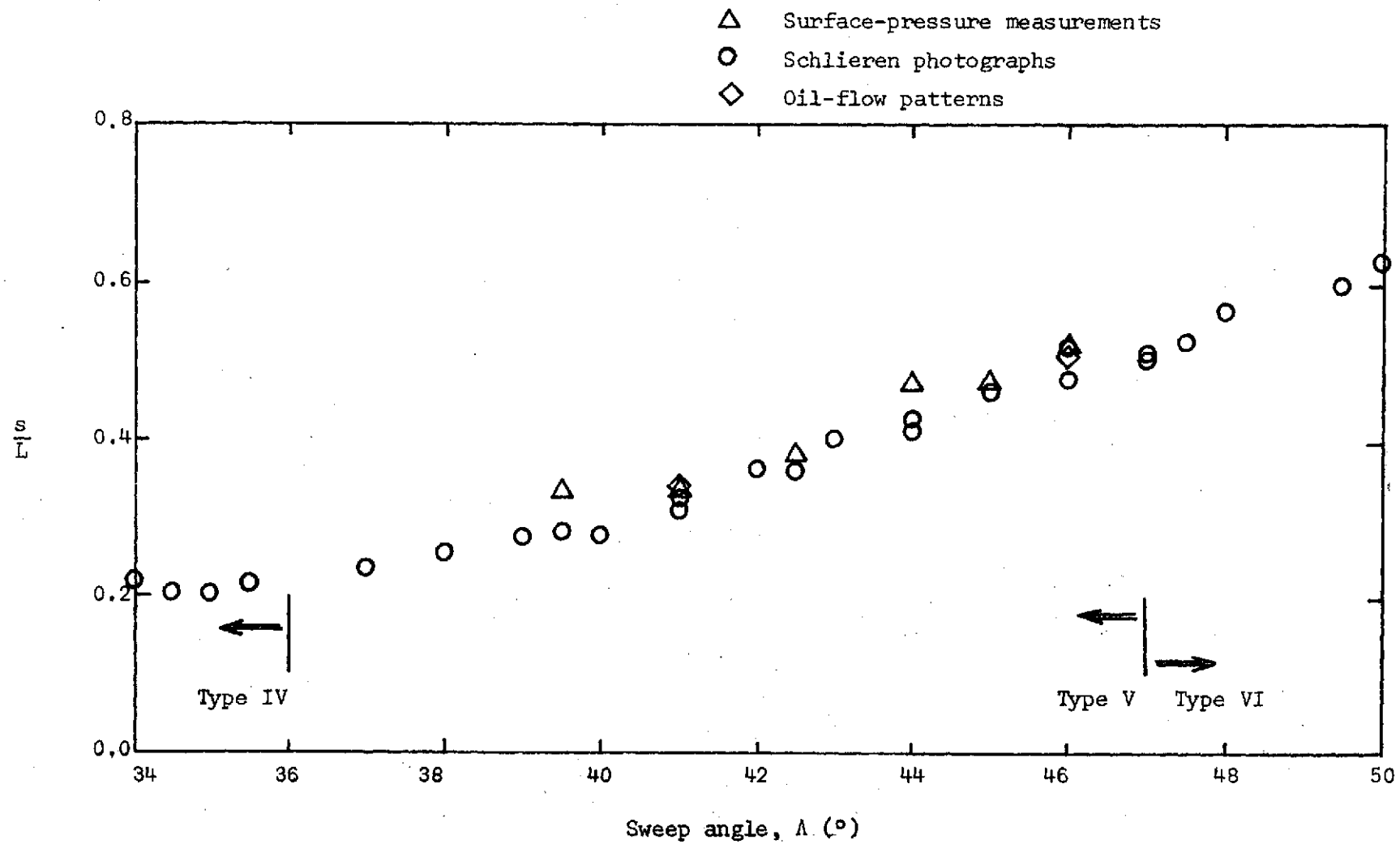
Figure 14. - Location of interaction perturbed region as a function of sweep angle (δ = 15°).
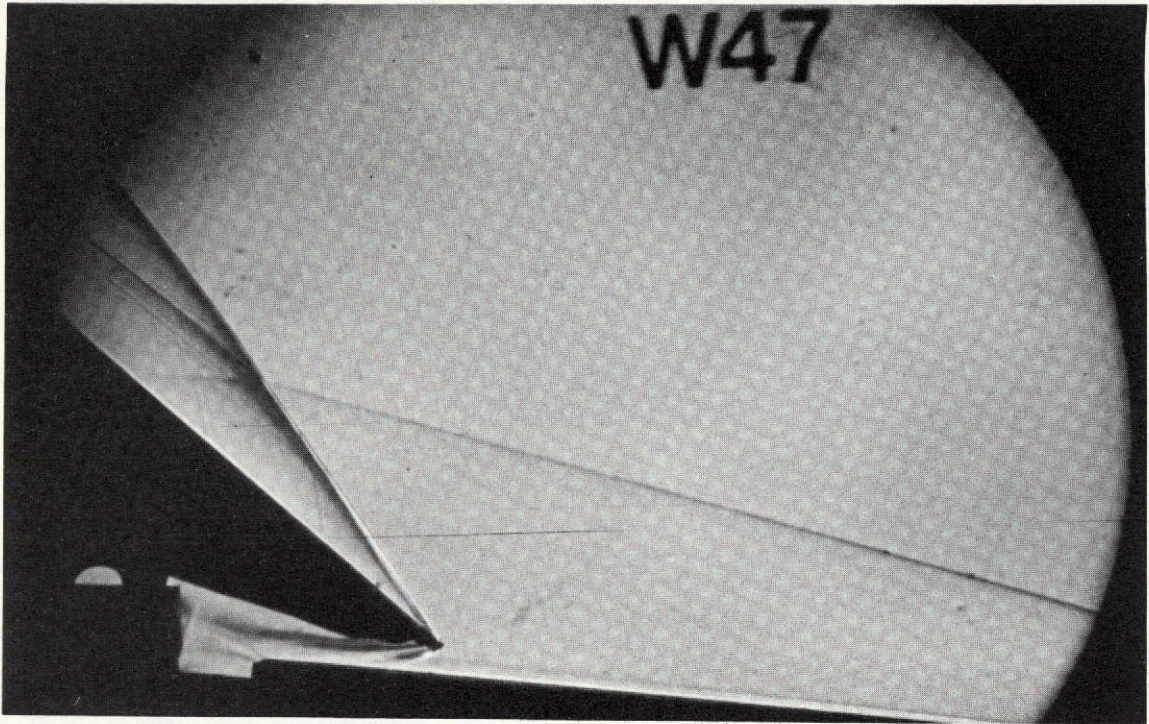
(a) Run W47, $\delta = 5°$, $\Lambda = 50°$
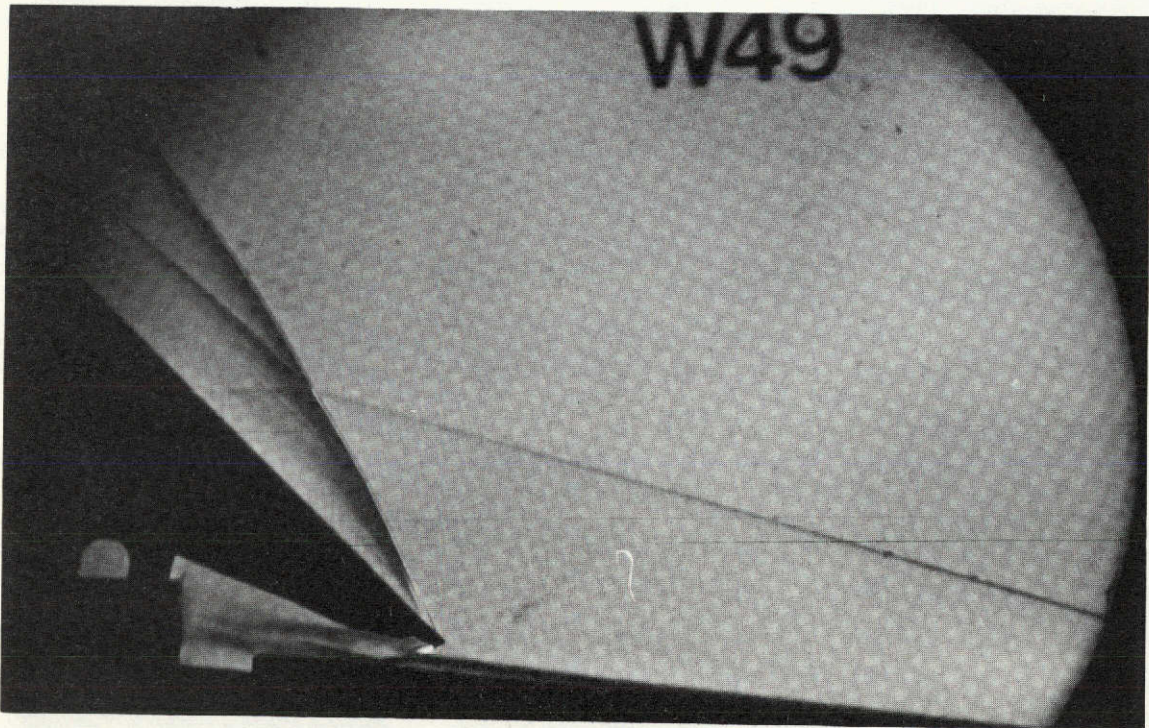
(b) Run W49, $\delta = 5°$, $\Lambda = 46°$

Figure 15. - Schlieren photographs of the shock-interference patterns over a range of sweep angles, $\delta = 5°$.

(c) Run W53, δ = 5°, Λ = 43°
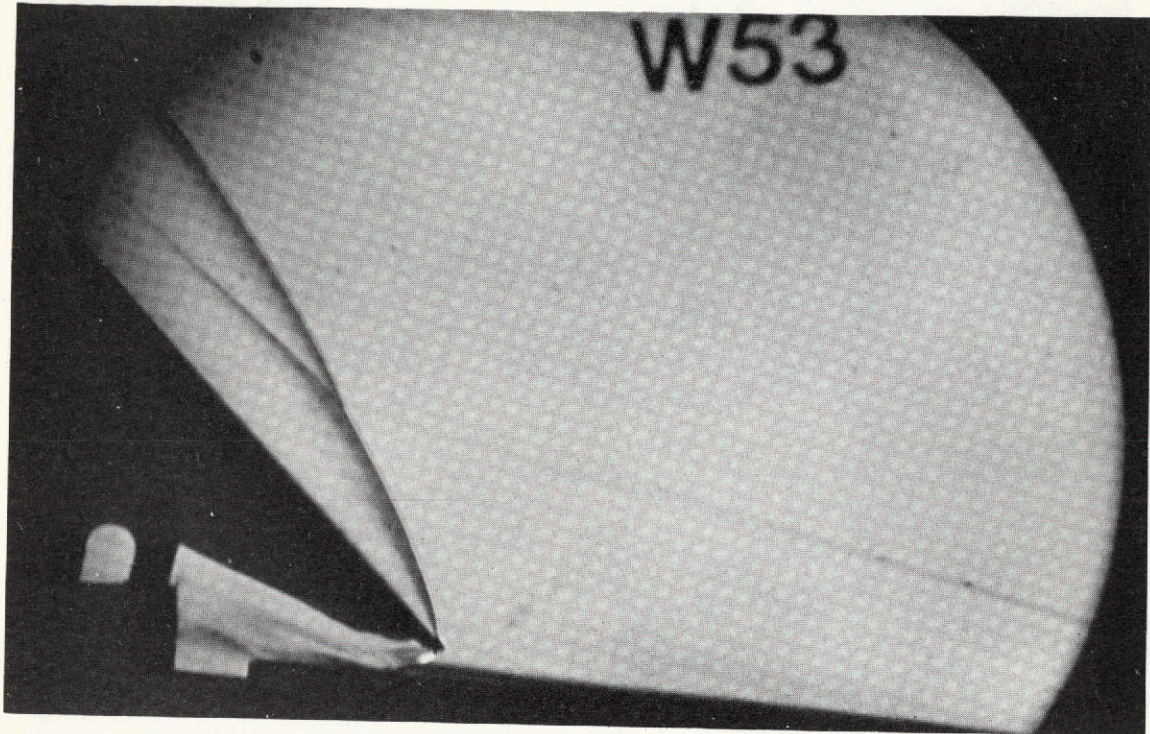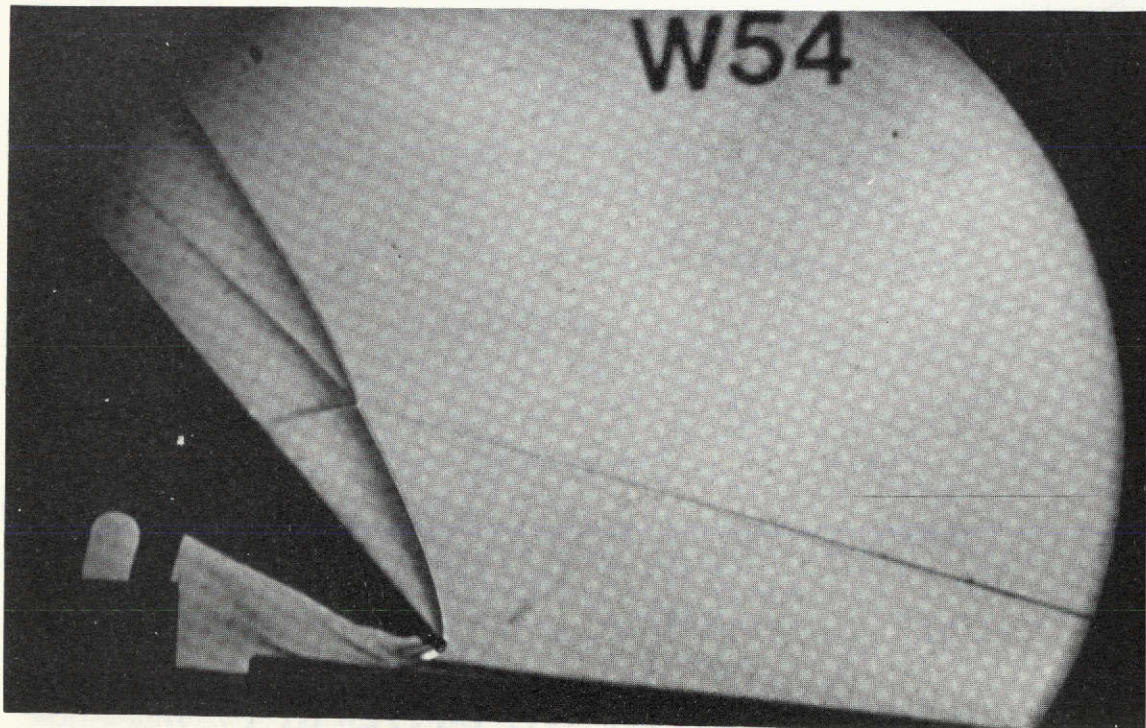
(d) Run W54, δ = 5°, Λ = 41.5°

Figure 15. - Continued.

45
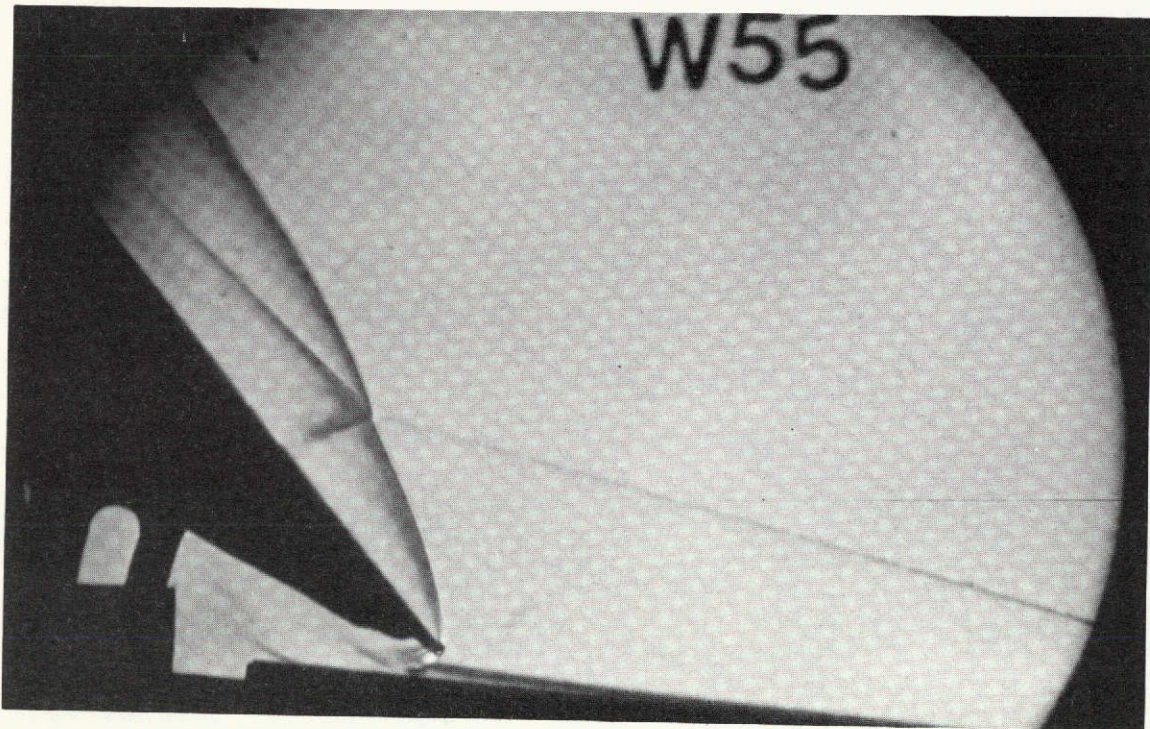
(e) Run W55, $\delta = 5°$, $\Lambda = 40°$

Figure 15. - Concluded.

$\dfrac{y}{L}$ ○ 0.0000   △ 0.1791
         ◇ 0.0597   △ 0.2388
         □ 0.1194

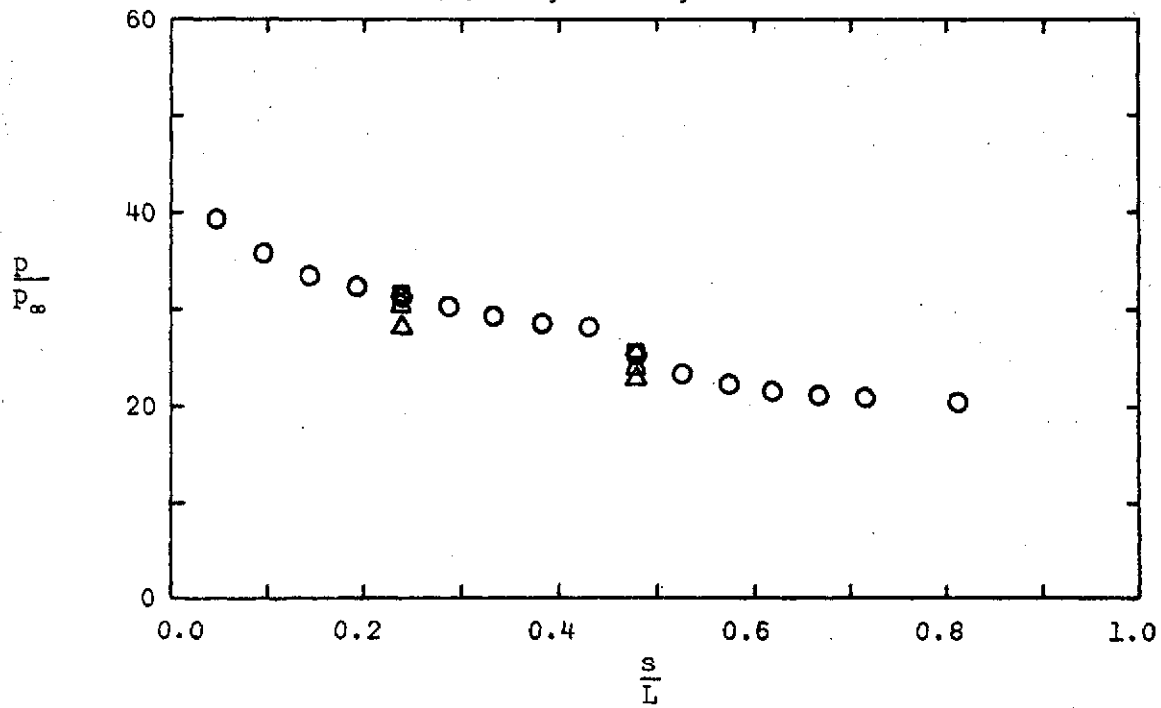(a) Run W47, $\delta = 5°$, $\Lambda = 50°$

(b) Run W49, $\delta = 5°$, $\Lambda = 46°$
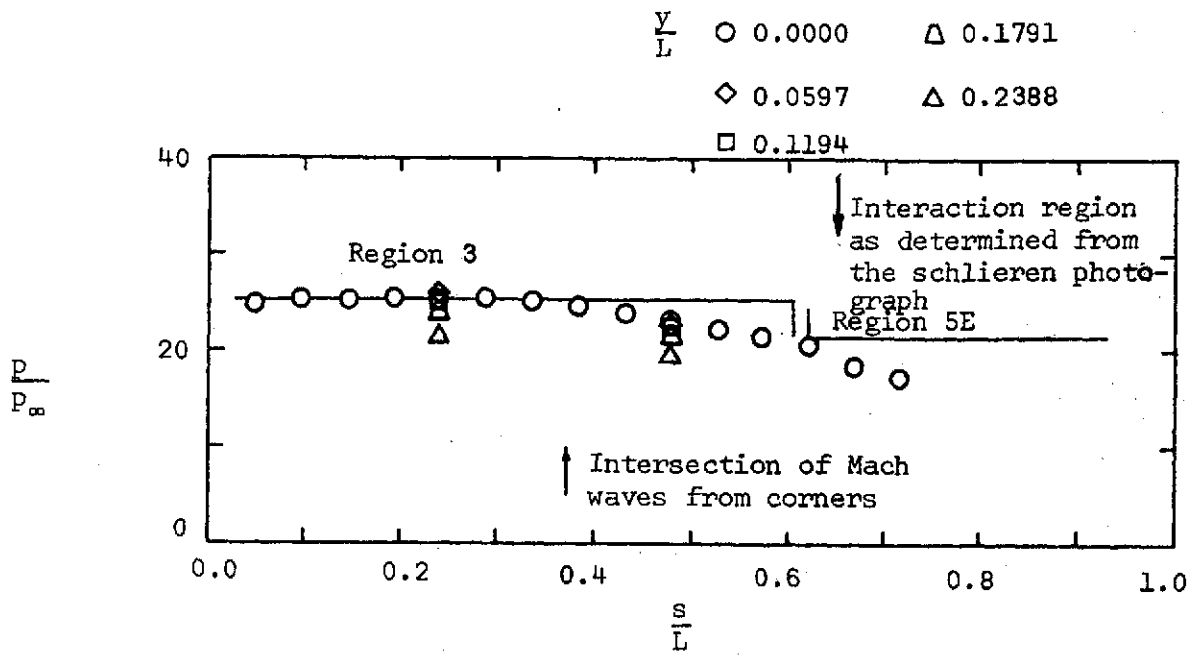
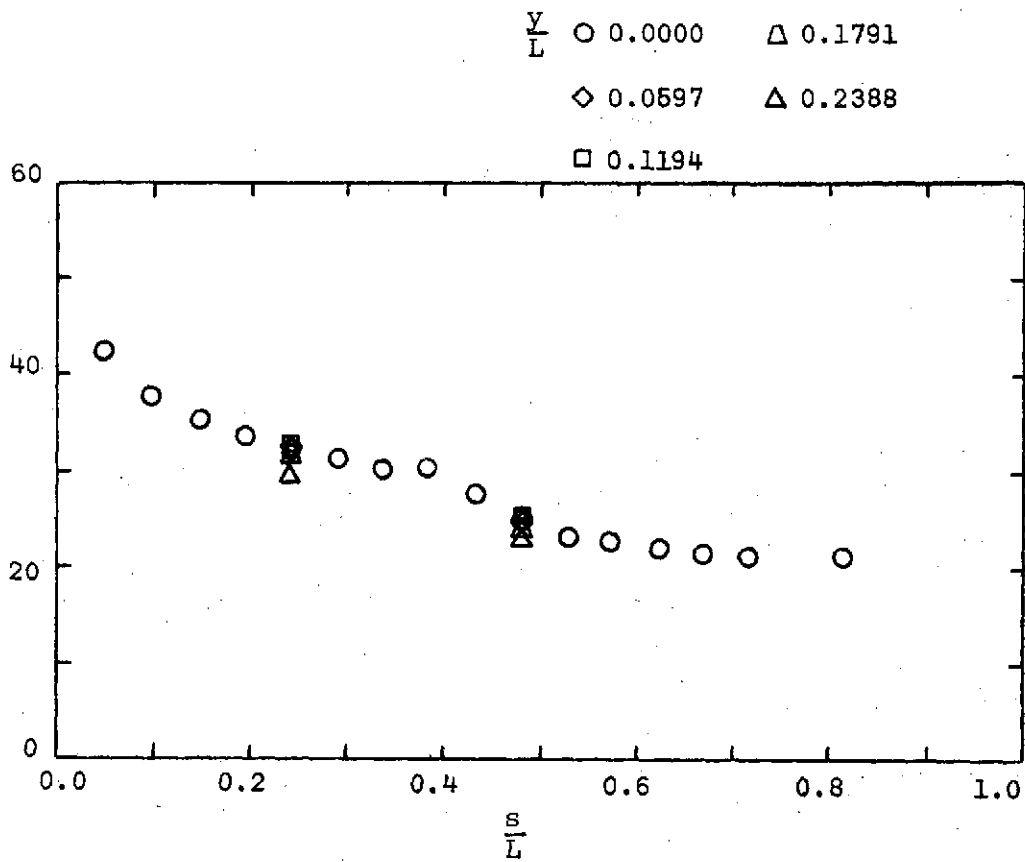Figure 16. - The pressure distribution along the simulated wing leading edge for several sweep angles ($\delta = 5°$).
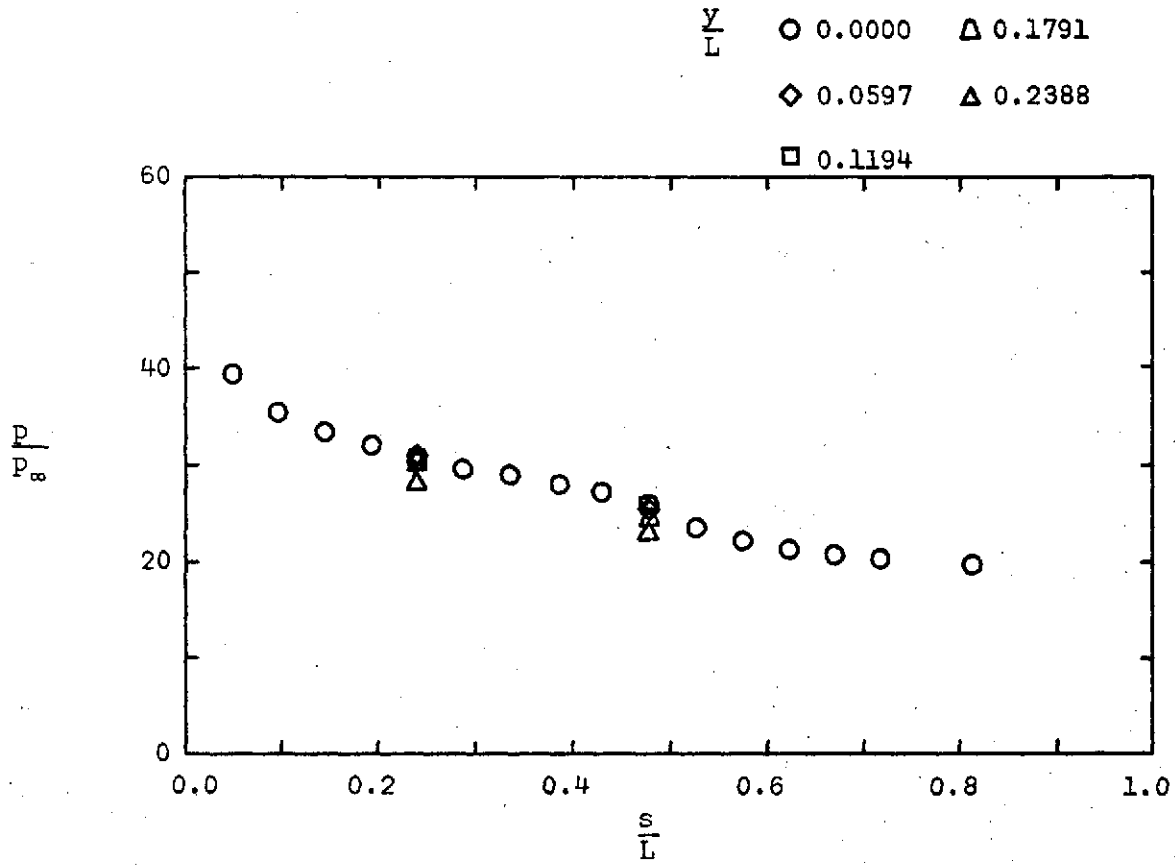
(c) W53, $\delta = 5°$, $\Lambda = 43°$

(d) W54, $\delta = 5°$, $\Lambda = 41.5°$

Figure 16. - Continued.

(e) Run W55, $\delta = 5°$, $\Lambda = 40°$
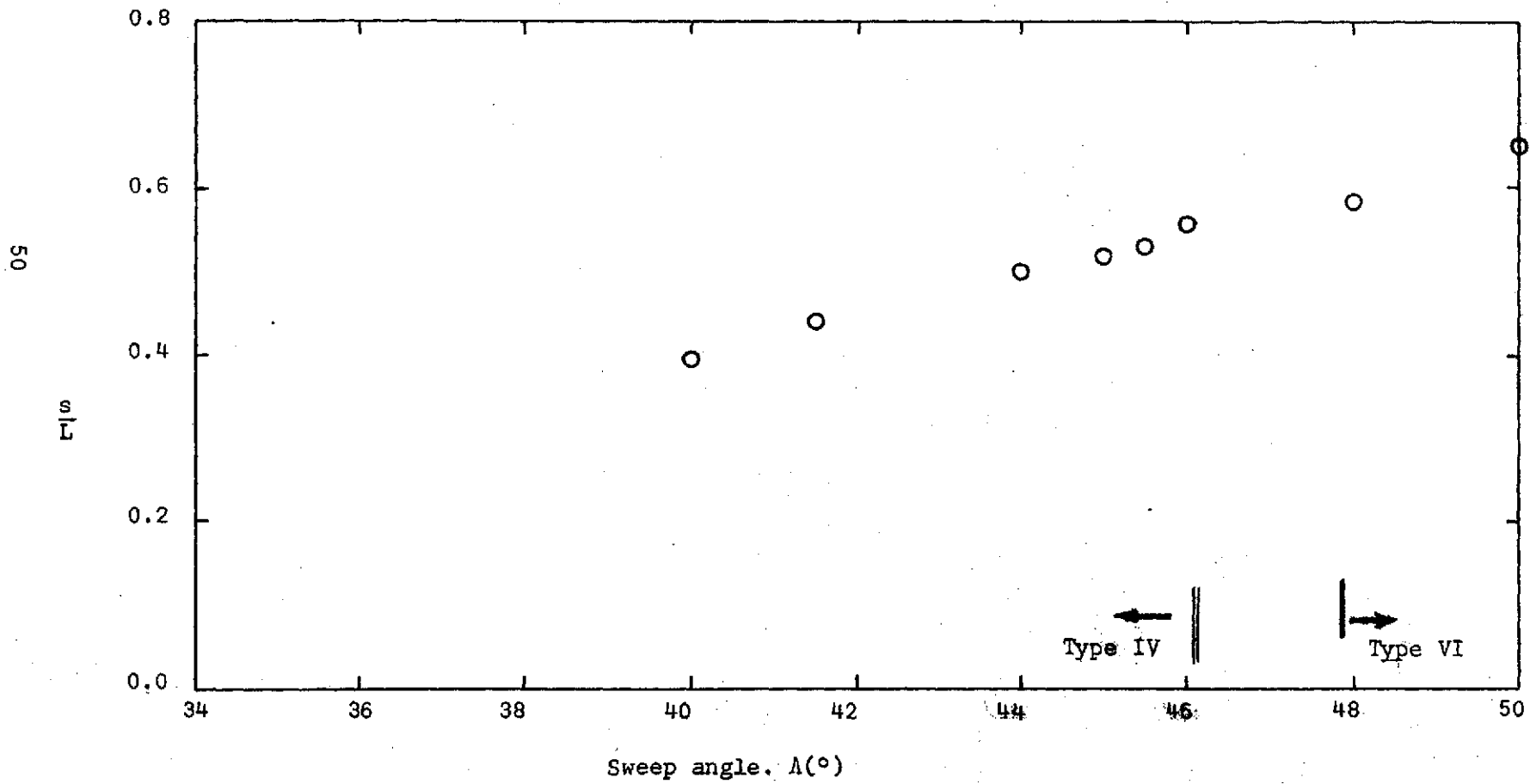
Figure 16. - Concluded.

Figure 17. – Location of the interaction perturbed region as a function of sweep angle for $\delta = 5°$.